

# Critical Evaluation of Quantum Machine Learning for Adversarial Robustness

Saeefa Rubaiyet Nowmi\*, Jesus Lopez\*, Md Mahmudul Alam Imon\*

Shahrooz Pouryousef†, Mohammad Saidur Rahman\*

\*Department of Computer Science, University of Texas at El Paso, El Paso, TX, USA

Email: {srnowmi, lopez126, mimon}@miners.utep.edu, msrahman3@utep.edu

†Computer Sciences, University of Massachusetts Amherst, Amherst, MA, USA

Email: shahrooz@cs.umass.edu

**Abstract**—Quantum Machine Learning (QML) integrates quantum computational principles into learning algorithms, offering the potential for improved representational capacity and computational efficiency. Nevertheless, the security and robustness of QML systems remain largely underexplored, particularly under adversarial conditions. In this paper, we present the first comprehensive systematization of adversarial robustness in QML, integrating conceptual organization with empirical evaluation across three threat models- black-box, gray-box, and white-box. We implement representative attacks in each category, including label-flipping for black-box, QUID an encoder level data poisoning for gray-box, and FGSM and PGD for white-box, using Quantum Neural Networks (QNNs) trained on two datasets from distinct domains, MNIST from computer vision, and AZ-Class from Android malware, across multiple circuit depths (2, 5, 10, and 50 layers), and two encoding schemes (angle and amplitude).

Our extensive evaluation shows that *amplitude encoding* yields highest clean accuracy (93% on MNIST and 67% on AZ-Class) in deep and noiseless circuits, however, it degrades sharply under adversarial perturbations and depolarization noise ( $p = 0.01$ ), reducing accuracy to below 5%. In contrast, *angle encoding* while offering lower representational capacity, remains substantially more stable in shallow, noisy regimes, revealing a clear trade-off between representational capacity and robustness. Furthermore, the QUID attack achieves higher attack success rates, though quantum noise channels disrupt the Hilbert-space correlations exploited by QUID, thereby weakening its impact in image domain. This observation suggests that noise can act as a natural defense mechanism in Noisy Intermediate- Scale Quantum (NISQ)-era quantum systems. We conclude by proposing a threat-aware and noise-resilient design framework for developing secure and robust QML systems.

**Index Terms**—Quantum Machine Learning; Adversarial Robustness; Evasion Attacks; Poisoning Attacks;

**Reproducibility.** Code is available at <https://github.com/IQSeC-Lab/SoK-QML>.

## I. INTRODUCTION

Quantum Machine Learning (QML) leverages fundamental quantum phenomena such as superposition, entanglement, and interference to explore potential for *quantum advantage* over Classical Machine Learning (CML) [1]–[6]. QML techniques have been investigated across diverse domains including combinatorial optimization [7], cybersecurity [8], [9], drug discovery [10]–[12] and so on. As QML transitions from theoretical

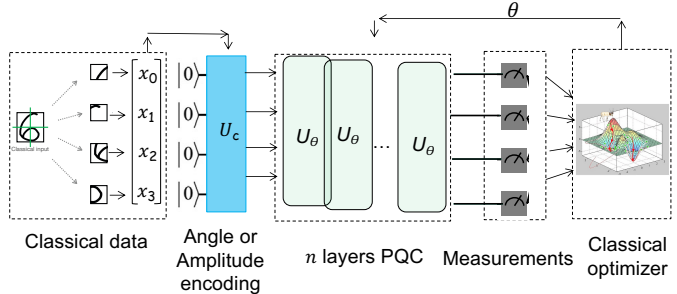


Fig. 1: Architecture of Parameterized Quantum Circuit (PQC) as a QML model. The circuit comprises three key components: (1) data encoding layers that map classical inputs into quantum states, (2) parameterized quantum gates that define the model’s behavior and are iteratively optimized, and (3) measurement operations that extract classical information for loss evaluation.

exploration to practical implementation [4]–[6], [13], the absence of a systematic understanding of adversarial robustness poses a critical barrier to their trustworthy deployment.

The emergence of cloud-based quantum computing services such as IBM Quantum [14], Amazon Braket [15], and Microsoft Azure Quantum [16] has accelerated the accessibility and scalability of QML. However, it has also broadened the attack surface [17]–[20]. Multi-tenant infrastructures, remote execution APIs, and shared quantum backend introduce novel vulnerabilities including crosstalk [19], [21], data leakage [22], and side-channel exposure [21]–[23], undermining the assurance of confidentiality and model integrity. Moreover, the hybrid architecture of QML as illustrated in Figure 1, which couples quantum and classical components, introduces complex dependencies across the software-hardware stack [24]. As such, QML systems inherit CML vulnerabilities and exhibit poorly understood quantum-specific threats.

Recent studies have demonstrated that QML models are vulnerable to both *training* and *inference* time attacks including evasion [25], [26], poisoning [27], backdoor [28]–[30]. In addition to the algorithmic attacks, hardware-level vulnerabilities have also been identified in Noisy Intermediate-Scale Quantum (NISQ) systems, such as state-leakage [23], [31], crosstalk [21], [32]–[34], power and timing side channel leakage [22], [35]–[38], and fault and pulse level manip-

ulations [39], [40]. These findings expose the fragility of QML’s security landscape and highlight the urgent need for a *systematic understanding of adversarial robustness in quantum learning systems*.

To address this gap, we propose a Systematization of Knowledge (SoK) that consolidates the research on QML adversarial robustness, develops an empirical framework for evaluating real-world vulnerabilities, and outlines a road-map towards secure and resilient QML. Towards that end, this work is driven by three fundamental research questions for systematization and empirical validation:

- RQ1 What are the dominant threat vectors in hybrid quantum-classical architectures, and how can they be systematically classified to capture both classical and quantum-specific adversarial capabilities?
- RQ2 How do *circuit depth* and *data encoding* influence the performance and adversarial robustness of *Parameterized Quantum Circuits* (PQCs) within the constraints of NISQ-era hardware?
- RQ3 To what extent are the current QML models and defense mechanisms resilient against respective attacks spanning black-box, gray-box, and white-box threat models compared to CML models?

Addressing these questions is critical for bridging the gap between theoretical advancement in QML and its secure, practical deployment. To this end, we structure our study in four stages. First, to explore RQ1, we construct a hybrid quantum-classical pipeline representative of model Quantum-as-a-Service (QaaS) platforms (e.g., IBM Quantum, Amazon Braket, and Microsoft Azure Quantum). These multi-tenant cloud environments inherently expand the attack surface by combining classical and quantum components. As such, we develop a *taxonomy of QML threat models*, presented in **section III**, categorizing adversarial capabilities into black-box, gray-box, and white-box levels, to enable systematic reasoning about vulnerabilities across the hybrid stack.

Secondly, to investigate RQ2, in **section V-A**, we analyze Quantum Multilayer Perceptron (QMLP) Architecture with two canonical data encoding schemes- angle and amplitude encoding and varying circuit depths (2, 5, 10, and 50 layer PQCs), to realize how architectural parameters shape accuracy, efficiency, and adversarial robustness under NISQ constraints.

To answer RQ3, in **section V-B**, **V-C** and **V-D**, we empirically implement one representative attack from each threat model category to evaluate the resilience of QML models and the effectiveness of existing defenses.

These attack-defense implementations are chosen for their prevalence and demonstrated impact on prior QML security research [25]–[27], [41], [42]. From the black-box threat model, we examine the *data poisoning (label flipping)* [43] attack and apply *label smoothing* [44] as its defense mechanism. For the gray-box threat model, we implement the *Quantum Indiscriminate Data Poisoning (QUID)* attack [27] and evaluate the *Q-Detection* defense [45]. Finally, from the white-box threat model, we examine gradient-based adversarial evasion

attacks using *Projected Gradient Descent (PGD)* [46] and the *Fast Gradient Sign Method (FGSM)* [47]. We do not replicate the attacks and defenses exactly as presented in prior literature; instead, we analyze and adapt them within the context of our experimental framework to ensure consistency and comparability across evaluated settings.

Finally, we distill our empirical findings into *practical design principles* for developing secure, noise-aware, and resilient QML pipelines tailored to NISQ-era constraints, bridging the gap between theoretical potential and real-world security assurance.

Given the growing importance of secure quantum learning systems, this work presents both a systematization and an empirical investigation of adversarial robustness in QML. Our main contributions are summarized as follows:

- We present a comprehensive systematization of adversarial attack models in QML, categorized by the adversary’s level of access.
- We empirically analyze how data encoding schemes (angle vs. amplitude) and circuit depth (2, 5, 10, and 50 layers) influence QML model performance and robustness under NISQ constraints. We find that under noiseless conditions, amplitude-encoded deep QMLP models outperform angle-encoded QMLPs, whereas under noisy conditions, shallow angle-encoded QMLPs exhibit superior robustness.
- We perform a comparative study with classical machine learning models, such as CMLPs (Classical Multilayer Perceptron), to highlight distinctive vulnerability patterns and motivate the need for quantum-specific defenses.
- We implement representative attacks and corresponding defenses across black-box, gray-box, and white-box threat models to evaluate the robustness of QML models, compare against to CML models, and assess the effectiveness of existing defense mechanisms. We find that QMLP models are more robust against classical label-flipping attacks but substantially more vulnerable to gradient-based perturbation attacks.
- We propose a structured design pipeline for developing secure and robust QML models integrating threat modeling, encoding strategy selection, and robustness evaluation under quantum noise.

To ground our systematization, we curate research works from leading security—IEEE S&P, ACM CCS, USENIX Security, and NDSS, published between 2020 and 2025, complemented by additional works from prominent venues for quantum related research such as Nature, Science, Nature Reviews Physics, npj Quantum Information, and Physical Review, and for machine learning research such as NeurIPS, IJCAI, and ICML.

## II. PRELIMINARIES

This section introduces essential background concepts for this work. We first review the fundamentals of quantum computation, including qubits, quantum gates, and their mathematical representations. We then summarize key ideas in

QML, covering hybrid quantum-classical models and variational circuits, followed by a brief discussion of noise models and limitations in current NISQ devices.

### A. Qubits and Gates

Quantum computing operates on *qubits*, the quantum counterparts of classical bits. Unlike classical bits that are either 0 or 1, a qubit can exist in superposition of states:

$$|\psi\rangle = \alpha|0\rangle + \beta|1\rangle, \quad (1)$$

where  $\alpha, \beta \in \mathbb{C}$  and  $|\alpha|^2 + |\beta|^2 = 1$ . Measurement collapses the state to  $|0\rangle$  or  $|1\rangle$  with corresponding probabilities  $|\alpha|^2$  and  $|\beta|^2$ .

Quantum operations are performed using *unitary gates*, which preserve normalization. For an  $n$ -qubit system, a gate  $U \in \mathbb{U}(2^n)$  satisfies:

$$U^\dagger U = UU^\dagger = I, \quad (2)$$

where  $U^\dagger$  is the Hermitian adjoint and  $I$  is the identity. Common single-qubit gates include  $X, Y, Z, H, R_X(\theta), R_Y(\theta), R_Z(\theta)$ , while multi-qubit gates such as CNOT and CRX enable entanglement, an essential feature for quantum computation [48].

### B. Quantum Machine Learning (QML)

QML integrates quantum computing (QC) and machine learning (ML) to improve how algorithms learn from data [1]. A quantum state is represented as a vector of  $|\psi\rangle$  in a  $2^n$ -dimensional space for  $n$  qubits, where information can exist in multiple states at once, a property known as *superposition*. Quantum effects such as *entanglement* and *interference* allow computations that can explore many possibilities simultaneously [48]. This parallelism offers potential speedups for problems like optimization and pattern recognition that are central to ML [49].

Most practical QML systems use a *hybrid quantum-classical* approach. As shown in Figure 1, the quantum processor executes *Parameterized Quantum Circuits* (PQCs) that prepares parameterized quantum circuits that prepare quantum states  $|\psi(\theta)\rangle = U(\theta)|0\rangle^{\otimes n}$ , where  $\theta = (\theta_1, \dots, \theta_\ell)$  are trainable parameters and  $U(\theta)$  is unitary [50]. Measurement outcomes are sent to a classical optimizer which updates  $\theta$  to minimize a loss  $L(\theta)$  via

$$\theta^{(t+1)} = \theta^{(t)} - \eta \nabla_{\theta} L(\theta^{(t)}), \quad (3)$$

with learning rate  $\eta$ . The measurement-optimization process forms a *variational quantum circuit* (VQC) and is the foundation of algorithms such as variational quantum eigensolver (VQE) [51], quantum neural network [52], and quantum convolutional neural network (QCNN) [53].

A typical QML pipeline consists of three stages-data embedding, parameterized quantum gates, and measurement followed by classical postprocessing (See Figure 1).

1) *Data Embedding*: Classical input representation must be mapped into quantum states before processing by a QML model. This step, called *data embedding* or *quantum feature mapping*, is performed using parameterized quantum gates such as rotation gates  $R_X$  or  $R_Y$  [54]. The choice of embedding method directly affects performance, with trade-offs in qubit count, circuit depth, and noise. Two common approaches are *angle encoding* and *amplitude encoding*.

- **Angle Encoding**: In this scheme, each classical feature  $x_i$  is mapped to a rotation angle of a single-qubit gate [55]. For an input vector  $\vec{x} \in \mathbb{R}^N$ , rotation gates  $R_X(x_i)$  or  $R_Y(x_i)$  are applied to  $N$  qubits to prepare quantum state:

$$R_Y(x_i)|0\rangle \text{ or } R_X(x_i)|0\rangle.$$

This method is simple and hardware-efficient but requires at least one qubit per input feature ( $N \leq n$ ).

- **Amplitude Encoding**: In this method, the entire input vector is encoded into the amplitudes of a quantum state [55]:

$$|\phi\rangle = \sum_{i=0}^{N-1} x_i |i\rangle, \quad (4)$$

where  $|i\rangle$  are basis states of  $\log_2 N$  qubits. This method is qubit-efficient but harder to implement on NISQ hardware due to complex state preparation and noise sensitivity.

2) *Parameterized Quantum Gates*: After input embedding, the circuit applies trainable unitary operations called *variational layers* [56]. Each layer consists of parameterized single-qubit rotation gates  $R_X(\theta)$ ,  $R_Y(\theta)$ , and  $R_Z(\theta)$ , combined with multi-qubit entangling gates such as CRX or CNOT. These gates form a PQC where parameters  $\theta$  are initialized randomly and updated during training, enabling the model to learn transformations while maintaining unitarity.

3) *Measurement and Postprocessing*: After variational layers, the quantum circuit is measured in computational basis to obtain classical outputs. Each measurement corresponds to expectation value of a Pauli-Z operator [57].

$$z_i = \langle \psi(\theta) | Z_i | \psi(\theta) \rangle, \quad (5)$$

where  $z_i \in [-1, 1]$  represents the outcome associated with qubit  $i$ . The resulting vector  $\mathbf{z} = (z_1, \dots, z_n)$  forms the quantum feature representations passed to classical post-processing layers such as fully connected or softmax classifiers. Gradients with respect to circuit parameters  $\theta$  are computed using the parameter-shift rule or finite difference methods, and classical optimizers (e.g., Adam, SGD) update the parameters in a hybrid training loop [58], [59].

### C. Quantum Multilayer Perceptron (QMLP)

QMLP is a hybrid quantum-classical model for supervised learning that integrates PQC within a classical workflow [1]. Classical inputs  $\mathbf{x} \in \mathbb{R}^d$  are first encoded into quantum states using either *angle encoding* or *amplitude encoding*. To enhance representational robustness, same features can be re-encoded across layers through re-uploading, analogous to stacking layers in classical neural networks.

Following embedding, the state passes through variational layers with trainable single-qubit rotations and CRX entangling gates. The quantum output is measured via Pauli-Z expectation values producing a real-valued vector  $\mathbf{z} \in \mathbb{R}^n$  that serves as input to classical fully connected layer. The model is trained end-to-end using gradient-based optimization in a hybrid quantum-classical loop.

#### D. Quantum Noise and NISQ Constraints

Current NISQ devices suffer from decoherence, limited gate fidelity, and readout noise, all of which degrade circuit performance [60]. These imperfections are commonly modeled as *quantum noise channels* acting on a quantum state  $\rho$ . A general noisy process is expressed as a completely positive trace-preserving (CPTP) map:

$$\mathcal{E}(\rho) = \sum_k E_k \rho E_k^\dagger, \quad (6)$$

where  $\{E_k\}$  are Kraus operators satisfying  $\sum_k E_k^\dagger E_k = I$ . Typical single-qubit noise channels include:

- **Depolarizing noise:**

$$\mathcal{E}_p(\rho) = (1-p)\rho + \frac{p}{3}(X\rho X + Y\rho Y + Z\rho Z), \quad (7)$$

which replaces the qubit with a maximally mixed state with probability  $p$ .

- **Amplitude damping:** models energy relaxation with Kraus operators

$$E_0 = \begin{bmatrix} 1 & 0 \\ 0 & \sqrt{1-\gamma} \end{bmatrix}, \quad E_1 = \begin{bmatrix} 0 & \sqrt{\gamma} \\ 0 & 0 \end{bmatrix}.$$

Noise accumulates with circuit depth, reducing fidelity and compounding the effects of adversarial perturbations.

### III. TAXONOMY OF ATTACK MODELS

In this section, we address **ROI** by presenting a *taxonomy* of adversarial threats in QML based on the adversary's level of access-black-box, gray-box, and white-box, and the quantum-specific mechanisms exploited during the attack. While prior works have explored individual attack scenarios [21], [27], [41], the absence of a unified framework has limited our understanding of how vulnerabilities propagate across different stages of the QML pipeline. We address this gap through our taxonomy, which highlights how each threat model maps to distinct attack categories such as *encoding manipulation* [27], *circuit tampering*, [26] and *hardware level side-channel attacks* [21]. This systematic classification also enables consistent comparison across existing literature and clarifies how classical attack paradigms extend into the quantum domain. Figure 2 illustrates the attack vectors within the QML workflow, and Table I summarizes representative attacks under each threat model. To operationalize this framework, we decompose the adversarial landscape along two key dimensions—the adversary's level of access and the nature of the exploited mechanism.

The first dimension-*access level*, captures the extent of the adversary's visibility and control over the QML workflow,

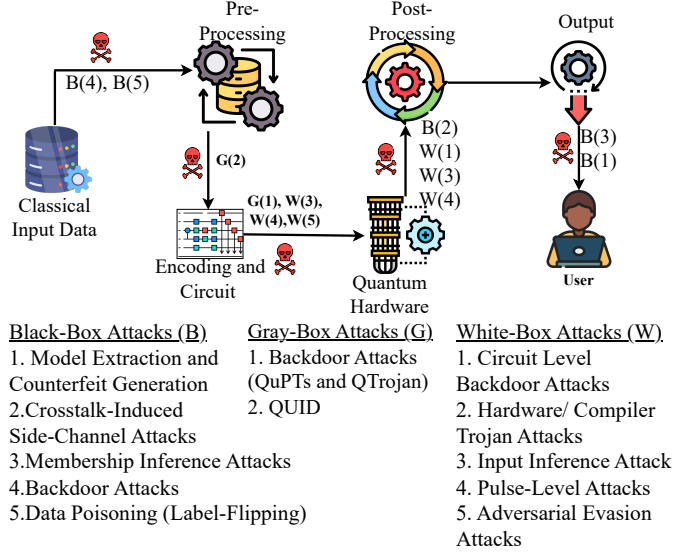


Fig. 2: Schematic representation of the adversarial attack deployment surface within the Quantum Machine Learning (QML) pipeline, illustrating potential threat vectors and their corresponding points of insertion. **(B)**: Black-Box, **(G)**: Gray-Box, **(W)**: White-Box.

defining three canonical threat models: *black-box* (query-only and third-party data access), *gray-box* (partial visibility into intermediate artifacts such as encoded states or transpiled circuits), and *white-box* (full access to parameters, architecture, and hardware). The second dimension distinguishes whether the attack leverages *classical-style manipulations* (e.g., data poisoning or gradient-based evasion) or *quantum-specific mechanisms* such as encoding interference, entanglement manipulation, or pulse-level perturbations. This dual-dimensional framework provides a unified lens for comparing classical and quantum vulnerabilities, illustrating how QML both inherits and extends traditional ML threats while introducing fundamentally new attack surfaces arising from quantum computation.

#### A. Black-Box Attack

In the *black-box* setting, the adversary has no internal visibility into the QML model's architecture, parameters, or hardware. Access is limited to model queries, typical of cloud-hosted QMLaaS or indirect influence on third-party data sources. This axis therefore represents the *lowest level of access*, yet attackers can still exploit both *classical-style manipulations* and *quantum-specific mechanisms* observable through system interfaces or shared resources [21], [40].

**Model Extraction and Counterfeit Generation.** A query-only adversary can approximate a target QML model by generating input-output pairs and training a local surrogate using these observations [61]–[63].

This classical-style manipulation enables functional replication and intellectual-property theft, allowing the attacker to reproduce decision boundaries or redeploy counterfeit models.

TABLE I: Systematization of Adversarial Attacks on QML according to Threat Models. Attacks empirically evaluated in this study are highlighted in green.

Threat Model	Attack Category	Related Paper	Attacker Profile	Target Artifacts	Capabilities
Black-box	Model Extraction & Counterfeit Generation	[61]–[63]	External adversary, co-tenant on multi-tenant NISQ hardware, malicious data contributor	Third-party Training Data, QML Outputs	Model Stealing, Functionality replication, Poisoning the data
	Crosstalk-induced Side-Channel	[21], [40]			
	Membership Inference	[64]			
	Black-Box Backdoor	[28], [29]			
	Data Poisoning (Label-Flipping)	[43], [44]			
Gray-box	Backdoor Attacks (QuPTs, QTrojan)	[30], [65]	Semi-privileged adversary, cloud provider	transpiled circuits, pre-execution artifacts, third-party training data	Manipulate inputs or IRs, estimate parameters or logic
	QUID	[27]			
White-box	Circuit-Level Backdoor	[66], [67]	Insider with full access (transpiler/infrastructure insider)	Transpiled gates, PQC, pulse schedule; parameters and gradients	Analyze and RE circuits, inject Trojan into hardware, Poison data in training time
	Hardware/Compiler Trojan	[68]			
	Input Inference	[69]			
	Pulse-Level Attack	[40]			
	Adversarial Evasion (FGSM/PGD)	[25], [26], [41]			

Such attacks compromise confidentiality and expose QML-as-a-Service providers to significant intellectual-property and usage risks.

**Crosstalk-induced side-channel attacks.** On multi-tenant NISQ devices, physical interference between qubits allows a co-resident attacker to observe correlated disturbances in *sensing* qubits and infer circuit activity or timing [21], [40]. This is a quantum-specific mechanism that reveals structural or operational metadata about the victim’s workload without direct access to its circuit or data. This vector principally undermines Confidentiality (leakage of circuit design and operational metadata) and can have secondary consequences for Integrity if reconstructed designs are misappropriated.

**Membership Inference Attacks.** In this black-box privacy threat, an adversary determines whether data sample was used during model training by comparing model’s confidence or output distribution across queries [64]. Such inference exploits overfitting and distributional biases to expose membership information, violating confidentiality even when models are deployed as restricted-access services.

**Backdoor Attack.** An adversary with limited influence over external training data can implant *universal quantum adversarial perturbations (QUAPs)* into a small subset of samples [28], [29]. After training, these perturbations reliably trigger targeted misclassifications while leaving clean inputs unaffected. This hybrid quantum–classical mechanism undermines integrity by introducing hidden, persistent backdoors that evade traditional validation procedures.

**Data Poisoning (Label-Flipping).** In a purely classical poisoning variant, the adversary contaminates third-party datasets by flipping labels for a subset of samples while leaving features unchanged [43]. This training-time corruption degrades model

accuracy and reliability, leading to global misclassification errors. We evaluate this in Section V-B, analyzing how encoding schemes and circuit depth influence robustness under noiseless and noisy conditions.

### B. Gray-Box Attack

In the gray-box setting, adversaries possess partial visibility into the QML system. They may access intermediate representations such as encoded quantum states, transpiled circuits, or compiler configuration files, but not the full model parameters or quantum hardware. This access level commonly arises in shared or outsourced computing environments such as compromised QaaS platforms or insider threats, where attackers can observe or slightly modify certain stages of the pipeline [27], [70]. Within this threat model, adversaries can combine classical control (e.g., data manipulation or configuration changes) with quantum-specific mechanisms (e.g., circuit injection or state perturbation) to degrade integrity or exfiltrate sensitive information.

**Backdoor Attacks (QuPTs and QTrojan).** Both the Quantum Properties Trojan (QuPT) and QTrojan operate under limited, pre-execution control of the victim’s workflow [30], [65]. The adversary modifies compiler configuration files or injects small, hidden gate fragments into encoding or variational layers before circuit compilation. QuPT leverages quantum properties such as  $U^\dagger U$  unitary pairs and ancilla triggers to amplify noise or distort superposition, whereas QTrojan employs pre- and post-encoding  $R_X/R_Y$  operations disguised as calibration routines. These attacks preserve simulation fidelity but activate malicious behavior on hardware, significantly reducing accuracy or forcing fixed misclassification. They primarily compromise integrity and availability while requiring no access to training data.

**Quantum Indiscriminate Data Poisoning Attack (QUID).** The QUID attack [27] illustrates how partial access to the quantum encoder suffices to corrupt learning. It exploits *Encoder State Similarity (ESS)*- the geometric closeness of quantum states in Hilbert space, to perturb labels and induce class confusion during training [71]–[73]. Unlike gradient-based classical poisoning, QUID manipulates quantum encodings directly, requiring minimal retraining or optimization overhead. Its impact stems from exploiting quantum geometry rather than statistical gradients, making it a uniquely quantum-specific attack. To mitigate this, Q-Detection [45] can be employed as a hybrid quantum-classical defense. We empirically evaluate QUID and Q-detection in section V-C.

### C. White-Box Attack

In the white-box setting, adversaries possess complete visibility and control over the QML system, including its architecture, parameters, compilation artifacts, and hardware execution stack [40], [66], [67], [74], [75]. This represents the highest level of adversarial access, encompassing malicious insiders, compromised service operators, or attackers with privileged control of the transpilation pipeline and backend hardware. Such adversaries can integrate classical-style manipulations. For example, gradient-based adversarial optimization with quantum-specific mechanisms such as pulse tampering, gate-sequence modification, or qubit remapping. This combination enables direct compromise of all three security properties- confidentiality, integrity, and availability, through parameter exfiltration, circuit modification, or disruption of quantum operations.

**Circuit Level Backdoor Attacks.** The adversary in a circuit-level backdoor attack scenario has full access to the transpiled, hardware-specific quantum circuit at inference time [66], [67]. The attacker parses the transpiled PQC and then modifies gate sequences, qubit mappings, or parameter placements. After making these changes, the adversary redeploys the altered circuit or pulse schedule on the target backend that force targeted misclassifications or leak quantum state information.

This attack compromises integrity and confidentiality while remaining difficult to detect, as changes occur after circuit verification but before hardware execution.

**Hardware/ Compiler Trojan Attack.** Adversaries with privileged access to the transpilation toolchain or backend configuration can implant malicious logic during compilation [68]. They modify coupling maps, insert stealthy ancilla-controlled gates, or adjust low-level pulse schedules. Such trojans can remain dormant in simulation but activate on real hardware, triggered by specific calibration parameters or device states. The result is persistent manipulation of outputs, exfiltration of model parameters, and degradation of hardware reliability, compromising the system’s confidentiality, integrity, and availability.

**Input Inference Attack.** An adversary with access to internal model parameters and gradients can reconstruct sensitive input data from training or inference phases [69]. By analyzing the

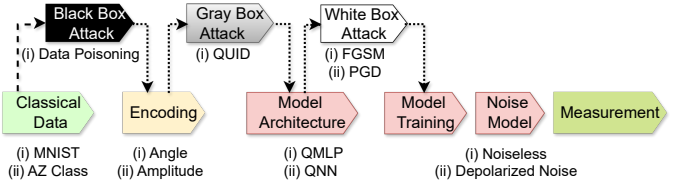


Fig. 3: Workflow Diagram of Experimental Setup.

mathematical relationships between parameters and encoded states, the attacker can infer original input features or their internal quantum representations. This privacy attack directly violates confidentiality and enables targeted manipulation in downstream tasks.

**Pulse-Level Attacks.** The pulse-level attack is a covert white-box or supply-chain threat in which an adversary with access to pulse definitions or the low-level control stack (i.e., compromised software development kits, gate-to-pulse mappers, or calibration tooling) tampers with waveform timing, phase, frequency, or amplitude to change hardware behavior without altering the gate-level circuit. The attack is deployed by inserting malicious pulse configurations or modifying custom-gate pulse files so that measurements, decoherence rates, or transient transitions are subtly and predictably altered. The attacker’s goals include forcing incorrect outcomes, embedding persistent backdoors, leaking quantum state information, or degrading device fidelity for later exploitation [40]. Such quantum-specific threats compromise confidentiality by leaking state information, integrity by forcing incorrect computations, and availability by destabilizing device performance.

**Adversarial Evasion Attacks.** With access to full model gradients and parameters, attackers can craft minimal perturbations to encoded inputs that cause targeted misclassification [25], [26], [41]. Methods such as FGSM and PGD modify input encodings or amplitudes, exploiting sensitivity in the parameterized quantum circuit. These classical-style evasion attacks highlight the fragility of QML decision boundaries under white-box conditions. We evaluate FGSM and PGD white-box attacks on our QMLP model using angle-encoding and amplitude-encoding in Section V-D.

## IV. EXPERIMENTAL SETTINGS

In this section, we outline datasets, model architectures, metrics, and computational framework for evaluation. We show a schematic representation of workflow in Figure 3.

### A. Dataset

We employ two multiclass datasets from distinct domains to evaluate adversarial robustness across vision and cybersecurity tasks. The first, MNIST [76], consists of ten handwritten digit classes representing image-based data, while the second, AZ-Class [77], comprises twenty-three Android malware families representing Android malware behavioral features in cybersecurity. This dual-domain setting enables cross-domain

evaluation of QML robustness under heterogeneous feature distribution

Our QMLP employs a 9-qubit circuit, which constrains the input dimensionality. Therefore, both datasets are reduced using *Principal Component Analysis (PCA)*, following prior QML practices [1]. For *angle encoding*, inputs are reduced to nine principal components (one per qubit), whereas for *amplitude encoding*, inputs are compressed to 512 dimensions to match the circuit's Hilbert space. This preprocessing ensures that feature representations align with the circuit's encoding capacity and NISQ hardware constraints. We utilize the full datasets, performing ten-class multiclass classification for MNIST and twenty-three-class multiclass classification for AZ-Class.

### B. Model Architectures

We have implemented QMLP models to analyze robustness against adversarial attacks under varying quantum conditions. Each QMLP follows a hybrid quantum-classical design in which the classical component is implemented in PyTorch and the quantum circuit is simulated using PennyLane's `default.qubit` backend [78]. To emulate realistic hardware behavior, depolarizing noise with probability  $p = 0.01$  is applied to single- and two-qubit gates ( $RX$ ,  $RZ$ ,  $X$ , and  $CX$ ) via the Qiskit Aer backend [79].

The QMLP architecture remains consistent across experiments, varying in circuit depth- 2, 5, 10, and 50 layers, and encoding strategy- angle and amplitude. All models are trained using Adam optimizer with learning rate 0.001, weight decay, and batch size of 64 for 30 epochs. For comparison with CMLP, we train a CMLP of similar architecture with similar training configurations. This enables a controlled analysis of whether observed vulnerabilities arise from quantum effects or from general learning dynamics.

### C. Baselines and Metrics

We define our *baseline models* as those trained without adversarial interference. They are trained under noiseless conditions and evaluated in both noiseless and depolarized environments ( $p = 0.01$ ). All attack and defense results are reported relative to these baselines.

Model performance is primarily evaluated using accuracy as the key metric. Additional performance measures, including the relative F1 score, false negative rate (FNR), and false positive rate (FPR), are reported in the Appendix. To assess robustness under attack, we use *relative accuracy*, defined as the ratio between the accuracy under attack and the clean (no-attack) accuracy. For any model,

$$\text{Relative Accuracy} = \frac{\text{Acc}_{\text{under attack}}}{\text{Acc}_{\text{baseline}}}.$$

Values close to 1 for relative accuracy indicate strong robustness, whereas smaller values reflect greater performance degradation under adversarial manipulation.

We maintained the same model architecture and evaluation metrics across all experiments, except for the gray-box QUID

attack and Q-Detection defense experiments. The experimental setups for these are discussed in Section V-C.

### D. Framework and Computational Resources

All experiments are performed using a hybrid PennyLane-PyTorch-Qiskit.Aer framework. Noiseless simulations are executed on NVIDIA H100 NVL GPUs (96 GB, CUDA 13.0), while noisy simulations using the `default.mixed` and `Aer` backends are run on multi-core CPUs due to the density matrix formalism. Depolarizing noise ( $p = 0.01$ ) is applied to single- and two-qubit gates to emulate NISQ behavior.

## V. EVALUATION

This section aims to systematically examine how *encoding schemes*, *circuit depth*, and *quantum noise* jointly influence model vulnerability, based on the dataset and experimental setup presented in the previous section, thereby addressing RQ2. We organize this section by evaluating each representative attack and its corresponding defense under controlled variations of encoding, circuit depth, and noise parameters, to address RQ3. For each threat model category (black-box, gray-box, and white-box), we analyze the impact of these factors on model robustness and discuss the resulting performance trends.

### A. Baseline

In this section, we report baseline performance for QMLP models under noiseless and noisy conditions, compared against a CMLP baseline. We analyze how encoding choice, circuit depth, and quantum noise affect accuracy and stability across datasets.

#### Key Insights: Baseline

- Encoding and circuit depth jointly determine QMLP performance; angle encoding favors shallow circuits (highest accuracy gain for 10 layer PQC), while amplitude encoding benefits from deeper ones.
- Noise severely limits model accuracy, with shallow angle-encoded circuits showing relatively higher resilience.

1) *QMLP with Noiseless Condition*: Table II presents the baseline performance of the QMLP models, while Figure 4 illustrates their accuracy progression over epochs. At shallow depths (2 layers), angle encoding performs better, achieving about 50% accuracy on MNIST and 49% on AZ-Class. This advantage arises from its localized qubit-wise mapping, which maintains stability when entanglement is minimal. However, as depth increases beyond ten layers, angle encoding degrades, falling to roughly 32% on AZ-Class, likely due to destructive interference and over-entanglement that hinder convergence. For angle encoding, 10 layer models achieve the highest accuracy in both the datasets.

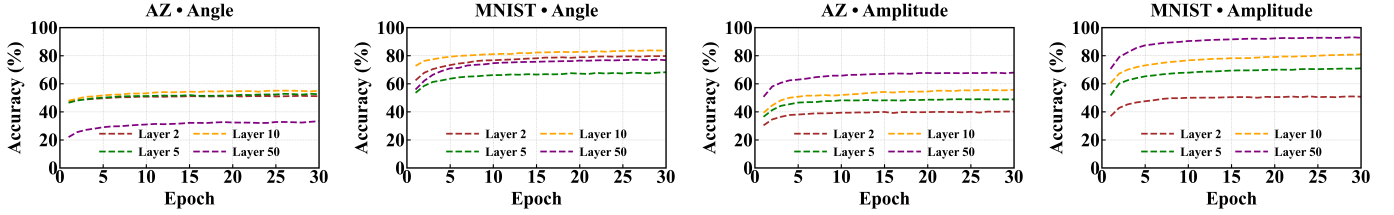


Fig. 4: Performance of the QMLP model with varying circuit layers and encoding schemes on the AZ-Class and MNIST datasets under a noiseless environment.

TABLE II: **Summary of Baseline Results.** Accuracies (%) of QMLP across encoding schemes and circuit depths for MNIST and AZ-Class datasets under noiseless and depolarized noise ( $p = 0.01$ ) conditions.

Encoding	Layers	Noiseless		Depolarized Noise	
		AZ-Class	MNIST	AZ-Class	MNIST
Angle	2	49.8	66.0	47.0	59.2
	5	52.3	68.0	22.4	45.0
	10	54.8	83.6	4.9	23.6
	50	32.4	76.9	5.2	9.9
Amplitude	2	40.1	50.7	5.1	9.9
	5	48.1	70.3	5.0	9.5
	10	55.0	79.8	4.78	10.1
	50	67.0	92.6	4.81	9.7

In contrast, amplitude encoding consistently improves with depth. Accuracy rises from around 50% at 2 layers to over 90% on MNIST and about 67% on AZ-Class at 50 layers. This pattern indicates that deeper amplitude-encoded circuits leverage the Hilbert-space representation more efficiently.

Overall, angle encoding gains modestly with depth, approximately 5-20%, while amplitude encoding improves dramatically, with up to 42% gains on MNIST and 27% on AZ-Class. These findings establish that *circuit depth is far more influential for amplitude-encoded models than for angle-encoded ones*. Additional results are provided in Appendix X-A, Table VII.

2) *QMLP with Depolarized Noise ( $p = 0.01$ )*: Table II also reports results under depolarizing noise, emulating NISQ-era conditions. For angle encoding, the 2-layer QMLP reaches 59% accuracy on MNIST, but performance declines to 9.9% at 50 layers as cumulative noise overwhelms coherence. For amplitude encoding, accuracy remains near 10% across all depths, indicating higher noise sensitivity. A similar pattern appears in AZ-Class results, where both encodings perform substantially worse than on MNIST. Additional results are provided in Appendix X-A, Table VIII.

3) *Classical Multi-layer Perceptron (CMLP) Model*: The CMLP baseline achieves 97% test accuracy on MNIST and 96% on AZ-Class (Appendix X-B, Table X). These results define upper performance bounds and underscore the gap between mature classical networks and current QML models. Unlike QMLPs, CMLPs are unaffected by quantum noise or circuit-depth limitations, highlighting that current NISQ

TABLE III: **Label-Flipping Attack.** All entries report *accuracy ratios* under label-flipping attacks relative to clean baselines. **N** = No Label Smoothing, **Y** = With Label Smoothing. **CMLP** baselines: 97% (MNIST), 96% (AZ-Class). **QMLP-Angle** and **QMLP-Amplitude** are Quantum MLPs using angle and amplitude encodings, respectively. **Acc.** = noiseless accuracy ratio; **AccDN.** = depolarized-noise accuracy ratio ( $p = 0.01$ ).

Model	Layers	LS	AZ-Class (ratio)		MNIST (ratio)	
			Acc.	AccDN.	Acc.	AccDN.
CMLP	—	N	0.51	—	0.50	—
	—	Y	0.59	—	0.51	—
QMLP-Angle	2	N	0.93	0.95	0.93	0.89
	5	N	0.91	1.73	0.95	1.00
	10	N	0.91	3.33	0.79	0.73
	2	Y	0.90	0.87	0.92	0.82
QMLP-Amplitude	5	Y	0.91	0.74	0.95	0.63
	10	Y	0.89	2.00	0.79	0.55
	2	N	0.94	1.10	1.03	0.98
	10	N	0.92	1.03	0.95	0.95
	50	N	0.93	1.00	0.97	1.02
	2	Y	0.87	1.02	1.06	1.01
	10	Y	0.91	1.05	0.98	0.99
	50	Y	0.90	0.98	0.97	1.05

constraints, not learning inefficiency, are the dominant cause of reduced quantum performance.

### B. Black-box $\rightarrow$ Data Poisoning (Label-Flipping)

#### Key Insights: Label-Flipping Attack

- QMLP models exhibit greater robustness than CMLP models under classical label-flipping attacks, despite the CMLP achieving higher accuracy.
- Classical defenses, such as *label smoothing*, do not provide any observable benefit for QMLP models, underscoring the need for quantum-specific robustness methods.

This attack simulates a training-time scenario where the attacker tampers with the dataset by flipping the labels of certain samples while keeping their features unchanged. The goal is to degrade model accuracy by misleading the training process. We implemented a 50% untargeted label-flipping

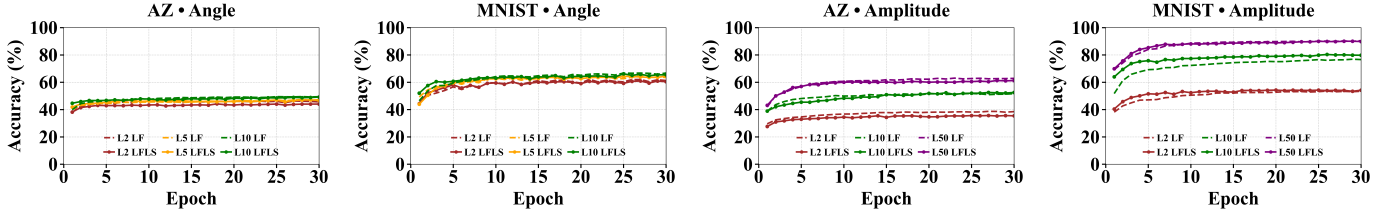


Fig. 5: Performance of QMLP under label-flipping (LF) and label-flipping with label-smoothing (LFLS) across datasets (AZ-Class, MNIST) and encodings (Angle, Amplitude) in noiseless conditions.

attack on QMLP models using both angle and amplitude encodings under noiseless conditions. For angle encoding, we evaluated 2, 5, and 10 layer circuits; for amplitude encoding, 2, 10, and 50 layer circuits. Angle encoding is more resource intensive than amplitude encoding, which made it infeasible to implement 50-layer models with angle encoding. All models are trained in noiseless conditions and tested under both noiseless and depolarizing noise ( $p = 0.01$ ), as shown in Table III. Inspired by classical machine learning defenses, we adopt *label smoothing* [44] with a smoothing factor of  $\alpha = 0.2$ , to mitigate the impact of label-flipping attacks by reducing the model’s overconfidence in corrupted labels. Figure 5 illustrates the test performance of QMLP models under noiseless conditions across epochs, comparing results with and without label smoothing.

1) *Performance under Noiseless Setting:* Both the angle- and amplitude-encoded QMLP models demonstrate strong robustness against label-flipping attacks across shallow and deep circuit configurations, with relative accuracies remaining close to 90% for both the AZ-Class and MNIST datasets. In contrast, the CMLP experiences a substantial degradation, losing nearly 50% of its accuracy relative to its clean performance. Classical label smoothing provides a modest improvement for CMLP across both datasets; however, the same strategy does not yield meaningful gains for QMLP models. These observations suggest that QMLP models exhibit greater robustness than classical models under data poisoning attacks; however, classical defense mechanisms fail to provide meaningful protection for QMLPs. This highlights the need for quantum-specific defense strategies that account for the unique properties and vulnerabilities of quantum learning architectures. Detailed results appear in Appendix X-C, Table XIV.

2) *Performance under Depolarizing Noise:* Under noisy conditions, angle-encoded QMLP models exhibit decreasing robustness as circuit depth increases, with a minor exception observed in the 5-layer configuration (without label smoothing) across both datasets. Except for the 10-layer QMLP models, all other configurations retain relative accuracies above 90%, indicating substantial resilience to label-flipping attacks even in the presence of noise. In several cases, the relative accuracy exceeds 1, suggesting that noise can weaken the influence of the poisoning signal as it disrupts the model’s learning process. even though the models show significant robustness, absolute accuracy drops sharply under noisy conditions, reflecting significant degradation in overall predictive

performance. Detailed results are presented in Appendix X-C, Table XV.

#### C. Gray-box $\rightarrow$ Quantum Indiscriminate Data (QUID) Poisoning Attack

##### Key Insights: QUID and Q-Detection

- QUID achieves up to 98.6% attack success outperforming random poisoning.
- Noise reduces QUID’s effectiveness by approximately 40% in the image domain (MNIST) and 18% in the malware domain (AZ-Class), highlighting its potential as a natural defense factor against encoder-level data poisoning attacks.
- Q-Detection offers limited protection, especially under noisy conditions.
- Even partial circuit access severely compromises model integrity.

QUID uses the concept of Encoder State Similarity (ESS) to modify training labels based on how close quantum states are in Hilbert space [27], [71]–[73]. The attacker perturbs the state encodings to cause class confusion and weaken the learning process. Unlike gradient-based classical poisoning, QUID does not require heavy retraining or optimization. It instead exploits the geometric relationships among quantum states to degrade performance with minimal effort.

To mitigate such poisoning, Q-Detection [45] proposes a hybrid quantum-classical defense that transforms the poisoning detection challenge to an optimization problem.

1) *Datasets and Pre-processing for QUID and Q-detection:* We conducted multiclass classification experiments on the MNIST image dataset and the AZ-Class malware dataset, each limited to the first four classes (0,1,2,3). For both datasets, 700 stratified samples per class were used for training and 300 for testing. Following the methodology of [27], we implemented a 4-qubit Quantum Neural Network (QNN) with angle encoding for 4-class classification to ensure experimental reproducibility. The datasets were subsampled rather than using all available samples, as the combined QUID [27] and Q-detection [45] framework is computationally intensive. For MNIST, each input was compressed into an 8-dimensional latent vector using a convolutional autoencoder following Kundu et al. [27], while the AZ-Class dataset was preprocessed by selecting the first four families, performing stratified sampling (700

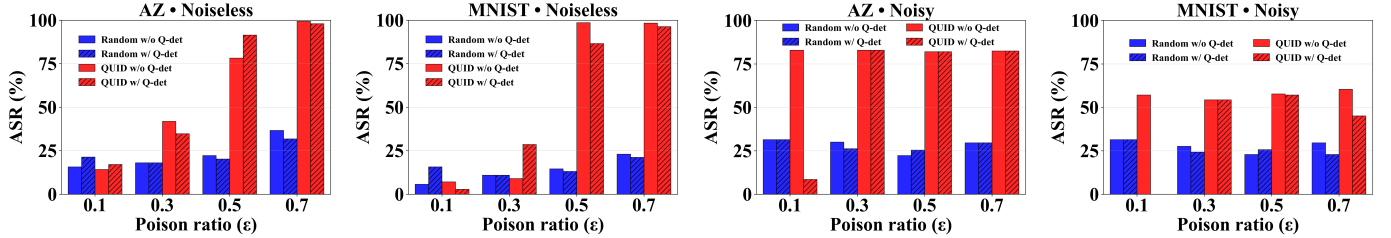


Fig. 6: Attack Success Rate (ASR %) over a range of poison ratios for the QNN under the QUID attack with and without Q-detection, evaluated on the MNIST and AZ-Class datasets.

training and 300 testing samples), and applying PCA-based dimensionality reduction with normalization to obtain latent features for model input.

2) *Model Architecture for QUID and Q-Detection:* Following [27], we implemented a 4-qubit hybrid Quantum Neural Network (QNN) using *angle encoding*, where each 8-dimensional latent input is scaled to  $[-\pi, \pi]$  and encoded via a sequence of single-qubit rotations- $R_Z(a)$ ,  $R_X(b)$ ,  $R_Z(a/2)$ , and  $R_X(b/2)$ -per qubit. The encoded state is then processed by a six-layer parameterized quantum circuit (PQC-6) [80] composed of  $R_Y$ ,  $R_Z$ ,  $R_X$ , and all-to-all entangling CRX gates to enhance circuit expressibility. The Pauli-Z expectation values from each qubit are passed to a classical linear layer for final classification.

Models were trained for 30 epochs with a batch size of 32, using the Adam optimizer ( $lr = 0.01$ ) under noiseless conditions. To emulate realistic NISQ noise, we used PennyLane’s `default.mixed` backend, introducing depolarizing and amplitude-damping noise channels after every single- and two-qubit gate with a probability of  $p = 0.05$ . The depolarizing channel randomizes qubit states to mimic control and gate imperfections, while the amplitude-damping channel models energy relaxation ( $T_1$  decay) and loss of coherence. Training under noisy conditions employed the Simultaneous Perturbation Stochastic Approximation (SPSA) optimizer (`spsa_stepsize = 0.01`, `spsa_perturb = 0.02`) to handle stochastic, non-differentiable gradients.

The Q-Detection defense [45] was integrated into the QNN training via a Quantum Weight-Assigning Network (Q-WAN), which dynamically reweights samples according to their training loss to suppress poisoned data influence. Following the original hyperparameter settings in [45], we used learning rate  $\eta = 0.05$ , annealing coefficient  $\alpha = 1.0$ , inverse temperature range  $\beta \in [0.1, 2.0]$ , and 50 annealing sweeps. Simulated annealing was adopted in place of quantum annealing to improve scalability while preserving functional parity with the original framework.

3) *Result and Analysis under Noiseless Setting:* As shown in Figure 6 and Table IV, we evaluate attack effectiveness using the Attack Success Rate (ASR)-the percentage of poisoned samples that cause misclassification.

Under the noiseless condition, and without any defense mechanisms in place, the QUID attack demonstrates a significantly higher ASR than the random label-flipping baseline

TABLE IV: QUID Attack Success Rate (ASR%) on AZ-Class and MNIST with and without Q-detection in noiseless settings. w/ Q-det: with Q-detection; w/o Q-det: without Q-detection.

Poison Ratio	Attack Type	AZ-Class (%)		MNIST (%)	
		w/o Q-det	w/ Q-det	w/o Q-det	w/ Q-det
0.1	Random	15.7	21.4	5.7	15.7
	QUID	14.3	17.1	7.1	2.9
0.3	Random	18.1	18.1	11.0	11.0
	QUID	42.0	34.8	9.0	28.6
0.5	Random	22.3	20.3	14.6	13.1
	QUID	78.3	91.4	98.6	86.6
0.7	Random	36.7	31.8	23.1	21.2
	QUID	99.4	98.0	99.0	96.3

across all poisoning ratios on both MNIST and AZ-Class datasets, except for the MNIST case at a poisoning ratio of 0.3, where the difference remains marginal. At higher poisoning ratios, QUID exhibits notably high ASR values, achieving 98.4% on MNIST (compared to 23.1% for random label-flipping) and 99.4% on AZ-Class (compared to 36.4% for random label-flipping) at a 0.7 poisoning ratio. These results clearly establish that QUID, and more broadly, encoder-level label-flipping attacks, are substantially stronger than conventional label-flipping attacks.

Furthermore, while Q-detection shows partial effectiveness in mitigating QUID’s impact, its performance does not follow a consistent pattern across datasets. In the image domain, Q-detection generally lowers ASR at higher poisoning ratios. Additional results in Appendix X-D, Table XVI, present QMLP classification accuracy under QUID attack with and without Q-detection in a noiseless environment.

4) *Result and Analysis under Noisy Setting:* Figure 6 and Table V present the ASR for QUID with and without Q-detection under noisy conditions. For the MNIST dataset, ASR decreases notably at higher poisoning ratios (0.5 and 0.7), showing an approximate 40% reduction at a 0.7 poisoning ratio compared to the noiseless case. Although ASR remains relatively higher at lower poisoning ratios (0.1 and 0.3), the overall variation between the highest and lowest ASR is only about 6%. This narrow margin suggests that, in the presence of noise, the model exhibits increased robustness, as higher poisoning ratios no longer lead to proportionally greater attack success. The AZ-Class dataset follows a similar trend, though

TABLE V: QUID Attack Success Rate (ASR%) on AZ-Class and MNIST with and without Q-detection in noisy settings. **w/ Q-det**: with Q-detection; **w/o Q-det**: without Q-detection.

Poison Ratio	Attack Type	AZ-Class		MNIST	
		w/o Q-det	w/ Q-det	w/o Q-det	w/ Q-det
0.1	Random	31.4	31.4	31.4	31.4
	QUID	82.9	8.6	57.1	0.0
0.3	Random	30.0	26.2	27.6	24.3
	QUID	82.9	82.9	54.3	54.3
0.5	Random	22.3	25.4	22.9	25.7
	QUID	82.0	82.0	57.7	57.1
0.7	Random	29.6	29.6	29.6	22.9
	QUID	82.4	82.4	60.4	45.1

the ASR drop is less pronounced (around 18% at 0.7).

Q-detection provides little improvement under noisy conditions. Moreover, model accuracy declines sharply in the noisy setting, as shown in Appendix X-D, Table XVII, consistent with the findings of [27].

#### D. White-box → Evasion Attacks

##### Key Insights

- Shallow angle-encoded QMLP models are more robust to FGSM and PGD attacks than deeper circuits.
- Amplitude-encoded models collapse under even small perturbations.
- CMLP models exhibit greater robustness against gradient-based perturbation attacks than QMLP models. .

As a representative white-box attack scenario, we evaluate both angle- and amplitude-encoded QMLP models under FGSM [26], [81] and PGD [26] attacks, varying perturbation magnitudes and circuit depths across multiple datasets. Both attacks are applied to models trained with MNIST and AZ-Class under noiseless conditions using angle and amplitude encoding.

TABLE VI: Relative accuracy under FGSM and PGD attacks for CMLP, QMLP–Angle(Angle), and QMLP–Amplitude (Amplitude). Ratios are  $\text{Acc}_{\text{attack}}/\text{Acc}_{\text{None}}$  for each model, dataset, and layer.

Layers	Attack	MNIST Ratio			AZ-Class Ratio		
		CMLP	Angle	Amp	CMLP	Angle	Amp
2	FGSM $\epsilon=0.01$	0.975	0.491	0.298	0.971	0.392	0.342
	FGSM $\epsilon=0.10$	0.327	0.050	0.099	0.295	0.317	0.017
	FGSM $\epsilon=0.15$	0.167	0.011	0.043	0.127	0.279	0.010
	PGD $\epsilon=0.01$	0.976	0.483	0.274	0.969	0.390	0.327
	PGD $\epsilon=0.10$	0.094	0.041	0.032	0.103	0.309	0.005
	PGD $\epsilon=0.15$	0.020	0.005	0.004	0.024	0.263	0.000
50	FGSM $\epsilon=0.01$	0.975	0.350	0.295	0.971	0.160	0.269
	FGSM $\epsilon=0.10$	0.327	0.074	0.000	0.295	0.154	0.000
	FGSM $\epsilon=0.15$	0.167	0.047	0.000	0.127	0.154	0.000
	PGD $\epsilon=0.01$	0.976	0.330	0.237	0.969	0.130	0.230
	PGD $\epsilon=0.10$	0.094	0.034	0.000	0.103	0.034	0.000
	PGD $\epsilon=0.15$	0.020	0.009	0.000	0.024	0.019	0.000

1) *FGSM and PGD Attacks in Noiseless Setting*: Figure 7 illustrates the accuracy of the QMLP model under the FGSM attack across different perturbation levels, while Figure 8 presents the corresponding accuracy under the PGD attack. Table VI summarizes the relative accuracy of the QMLP and CMLP models for the attacks. Additional results for  $\epsilon = 0.15$  and for models with 5 and 10 layers are provided in Appendix X-B.

Angle-encoded QMLP models exhibit moderate robustness at shallow circuit depths but degrade substantially as the number of variational layers increases. On the AZ-Class dataset, the 2-layer QMLP achieves a relative accuracy of 0.38 under a PGD attack with  $\epsilon = 0.01$ , whereas the 50-layer QMLP drops sharply to 0.12 under the same perturbation level. In contrast, the CMLP baseline maintains a much higher relative accuracy of 0.97 at  $\epsilon = 0.01$ . A similar trend is observed at higher perturbation strengths: at  $\epsilon = 0.10$ , the relative accuracy of the 2-layer QMLP is 0.31, but the 50-layer QMLP collapses to 0.03. For the same setting, the CMLP baseline records a relative accuracy of 0.09. These results indicate that CMLP models are considerably more robust than QMLPs under PGD attack. Moreover, the clear decline in relative accuracy with increasing depth shows that deeper angle-encoded QMLP architectures become progressively more fragile. The MNIST results follow the same overall pattern, reinforcing the depth-dependent robustness characteristics of angle-encoded QMLP models. All the models show the similar behavior under the FGSM attack as well.

For amplitude encoding, relative accuracies are substantially lower across all configurations, indicating that amplitude-encoded QMLP models exhibit limited robustness under PGD attack. For both datasets, performance deteriorates rapidly as perturbation strength increases: at  $\epsilon = 0.10$ , the relative accuracy is effectively zero for both shallow and deep circuits.

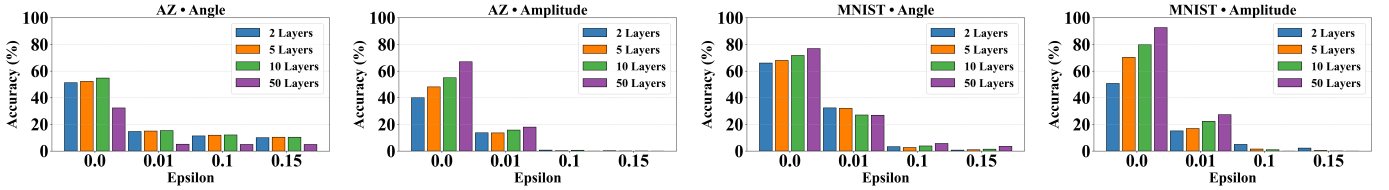


Fig. 7: Performance of QMLP with varying perturbation strengths of the FGSM attack in a noiseless environment.

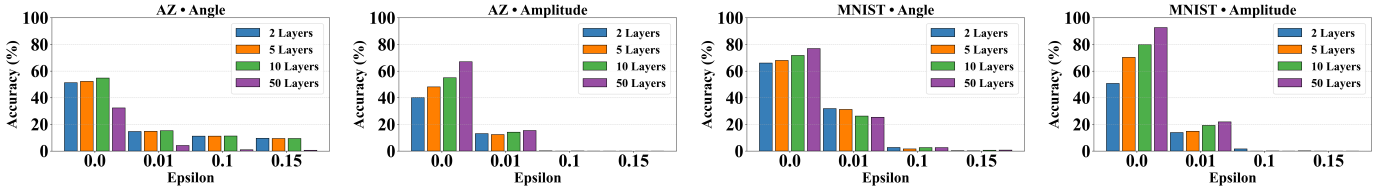


Fig. 8: Performance of QMLP with varying perturbation strengths of the PGD attack in a noiseless environment.

This near-complete collapse under higher perturbations suggests that amplitude-encoded QMLP architectures are highly vulnerable to adversarial noise and do not retain meaningful predictive capability in such settings. All models exhibit similar behavior under the FGSM attack as well.

Overall, shallow angle encoded QMLPs, demonstrate relatively higher stability under FGSM and PGD attacks, while deeper and amplitude-encoded circuits exhibit total collapse.

## VI. SECURE AND ROBUST QML PIPELINE DESIGN

In this section, we present a modular security framework for quantum machine learning (QML) systems, grounded in a well-defined threat model to address. We overview different security considerations from encoding and circuit architecture to training interfaces, hardware execution, and distributed deployment, and highlight concrete techniques for mitigating adversarial risk and preserving model integrity. Figure 9 illustrates the key defenses mapped to each stage of the QML pipeline design.

### Defining the Adversarial Threat Model.

As outlined in Section III, securing a QML pipeline begins with a precise threat model that defines the adversary's capabilities, access level, and objectives. A well-specified threat model anchors realistic security evaluation and determines which defenses are needed and where they should be applied. In the QML context, this requires accounting for the hybrid quantum-classical workflow and the physical constraints of NISQ hardware.

In practice, threat modeling involves identifying which components of the pipeline—such as encoded data, transpiled circuits, or pulse-level control signals—are observable or modifiable under each adversarial profile. This enables systematic mapping of feasible attack vectors and ensures that defenses target realistic risks rather than hypothetical extremes. A threat model aligned with our taxonomy thus serves as the foundation for secure QML design, ensuring that robustness assessments reflect plausible adversarial conditions and preventing both over- and under-provisioning of countermeasures.

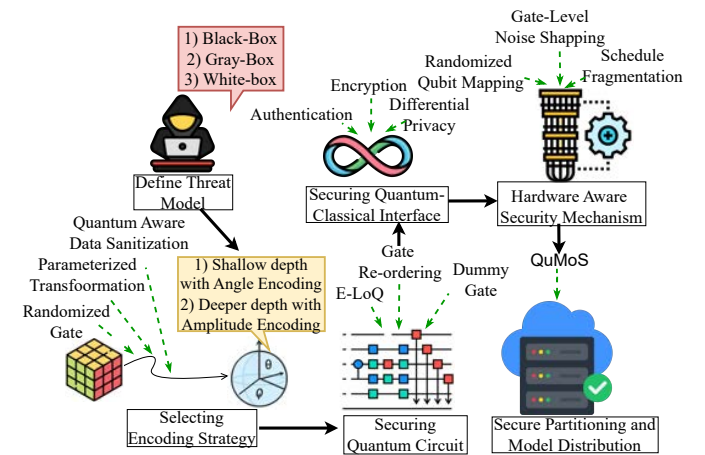


Fig. 9: Proposed Secure and Robust QML Pipeline.

**Encoder-Level Security Considerations.** The data encoding stage forms the first and one of the most critical interfaces between classical and quantum components in a QML pipeline. Adversaries with partial visibility into the encoding circuit can exploit this layer to infer sensitive information or introduce perturbations that compromise model integrity. Even small manipulations of amplitude or angle encoding parameters can distort state geometry in Hilbert space [27], leading to corrupted feature representations that propagate through the variational circuit.

To mitigate such risks, encoding procedures should incorporate quantum-aware validation [82]–[84], particularly against label poisoning attacks that exploit state similarity. Randomized or obfuscated encoding schemes [85], [86] can further reduce information leakage. Practical safeguards such as classical-quantum consistency checks, which compare reconstructed classical features against expected quantum states [87], help detect tampering and preserve encoding integrity.

### Securing Quantum Circuit Architecture.

Variational quantum circuits (VQCs) are prime targets for model extraction and reverse engineering [67]. Their confidentiality and structural integrity can be protected through quantum logic locking (QLL) [88], circuit obfuscation [86], [89], and secure training mechanisms. QLL embeds key-dependent behavior into circuit pathways, and the circuit functions correctly only when the valid secret key is supplied [88], [90]. Advanced schemes such as E-LoQ [91] encode multiple classical key bits into a single qubit, and this reduces overhead while increasing entropy.

Complementary obfuscation techniques, including gate reordering and insertion of dummy gates [92], introduce structural diversity that impedes static analysis and simulation-based reverse engineering. Together, these mechanisms strengthen the confidentiality of quantum circuit logic and hinder adversarial reconstruction of proprietary QML architectures.

**Hardware Aware Security Mechanism.** At the hardware layer, safeguarding QML workloads requires mechanisms that suppress crosstalk [32], [93], mitigate pulse-level interference [40], and preserve the confidentiality of quantum operations executed on shared or cloud-based devices.

Hardware-level defenses employ a combination of spatial, temporal, and signal-level countermeasures that collectively minimize information leakage. Randomized and dynamic qubit mapping [21] prevents adversaries from exploiting fixed spatial correlations in multi-tenant processors, while commutativity-based instruction reordering [94] and staggered scheduling desynchronize temporal patterns of entangling gates [95]. Dynamical decoupling sequences, implemented through control-pulse modulation, act at the hardware–firmware interface to suppress correlated noise and crosstalk-mediated leakage without requiring physical redesign [21], [96]. Complementary calibration-based defenses, including frequency detuning and adaptive recalibration, attenuate parasitic coupling between neighboring qubits and reduce electromagnetic interference across control lines [97]. At the signal layer, pulse-channel verification and noise shaping ensure the authenticity of microwave gate definitions and block unauthorized waveform manipulation during execution [40]. Finally, hardware noise fingerprinting, derived from device-specific calibration artifacts, provides a lightweight provenance mechanism for hardware authentication and tamper detection [98]. Together, these defenses strengthen the quantum hardware stack against side-channel attacks, preserving the integrity and confidentiality of QML workloads in NISQ-era systems.

**Secure Partitioning and Model Distribution.** To mitigate centralized deployment risks, QML models should adopt partitioning strategies like QuMoS [70], which divide functionality across multiple quantum backends. These isolated sub-circuits are individually non-informative and communicate via secure classical channels, reducing the risk of model reconstruction and supporting data locality and trust boundaries in federated settings.

## VII. PRACTICAL CHALLENGES AND LIMITATIONS

We conducted all experiments on a NVIDIA H100 NVL GPU node. However, due to the substantial computational demands of quantum machine learning (QML) models, we were unable to evaluate several configurations in this study.

First, we did not assess *randomized encoding* [85] as a defense mechanism. Preliminary tests showed that randomized gates significantly increased circuit depth and simulation overhead, making this approach impractical even with high-memory GPUs. We also excluded *label-flipping attacks* on 50-layer angle-encoded QMLP models. These deep circuits require repeated data re-uploading across variational layers, resulting in prohibitive runtime and memory usage under our hardware constraints. Furthermore, we could not evaluate FGSM and PGD attacks under *noisy* simulation. This limitation stems from software constraints. Current Qiskit-Aer backends do not support gradient computation in *noisy* mode, which is necessary for generating adversarial perturbations.

Finally, we restricted our experiments to 10-class MNIST classification and 23-class AZ-Class classification. Scaling to higher class counts caused exponential increases training time, exceeding the practical time budget within our available computational resources.

## VIII. CONCLUSION

In this work, we present the first comprehensive systematization of adversarial threats in quantum machine learning (QML), encompassing both classical-inspired and quantum-native attack vectors. Our results show that robustness of QML systems is significantly influenced by encoding strategies, circuit depth, and noise characteristics. Existing defenses remain limited in scope and are often constrained to simulation environments. As QML systems move closer to real-world deployment, there is a critical need to develop quantum-native robustness techniques, hardware-aware circuit designs, and formal threat models tailored to quantum architectures.

## IX. ETHICS CONSIDERATIONS

None

## REFERENCES

- [1] J. Biamonte, P. Wittek, N. Pancotti, P. Rebentrost, N. Wiebe, and S. Lloyd, “Quantum machine learning,” *Nature*, 2017.
- [2] H.-Y. Huang, M. Broughton, M. Mohseni, R. Babbush, S. Boixo, H. Neven, and J. R. McClean, “Power of data in quantum machine learning,” *Nature Communications*, 2021.
- [3] Y. Cao, J. Romero, J. P. Olson, M. Degroote, P. D. Johnson, M. Kieferová, I. D. Kivlichan, T. Menke, B. Peropadre, N. P. Sawaya *et al.*, “Quantum chemistry in the age of quantum computing,” *Chemical Reviews*, 2019.
- [4] W. Ren, W. Li, S. Xu, K. Wang, W. Jiang, F. Jin, X. Zhu, J. Chen, Z. Song, P. Zhang *et al.*, “Experimental quantum adversarial learning with programmable superconducting qubits,” *Nature Computational Science*, 2022.
- [5] H.-Y. Huang, M. Broughton, J. Cotler, S. Chen, J. Li, M. Mohseni, H. Neven, R. Babbush, R. Kueng, J. Preskill *et al.*, “Quantum advantage in learning from experiments,” *Science*, 2022.
- [6] V. Havlíček, A. D. Córcoles, K. Temme, A. W. Harrow, A. Kandala, J. M. Chow, and J. M. Gambetta, “Supervised learning with quantum-enhanced feature spaces,” *Nature*, 2019.

[7] X. Ye, G. Yan, and J. Yan, "Towards quantum machine learning for constrained combinatorial optimization: a quantum qap solver," in *International Conference on Machine Learning (ICML)*, 2023.

[8] A. Bellante, T. Fioravanti, M. Carminati, S. Zanero, and A. Luongo, "Evaluating the potential of quantum machine learning in cybersecurity: A case-study on PCA-based intrusion detection systems," *Computers & Security*, 2025.

[9] J. Lopez, S. R. Nowmi, V. Cadena, and M. S. Rahman, "Towards quantum machine learning for malicious code analysis," *arXiv preprint arXiv:2508.19381*, 2025.

[10] K. Batra, K. M. Zorn, D. H. Foil, E. Minerali, V. O. Gawriljuk, T. R. Lane, and S. Ekins, "Quantum machine learning algorithms for drug discovery applications," *Journal of Chemical Information and Modeling*, 2021.

[11] J. Li, M. Alam, M. S. Congzhou, J. Wang, N. V. Dokholyan, and S. Ghosh, "Drug discovery approaches using quantum machine learning," in *ACM/IEEE Design Automation Conference (DAC)*, 2021.

[12] M. Avramouli, I. K. Savvas, A. Vasilaki, and G. Garani, "Unlocking the potential of quantum machine learning to advance drug discovery," *Electronics*, 2023.

[13] D. Ristè, M. P. Da Silva, C. A. Ryan, A. W. Cross, A. D. Córcoles, J. A. Smolin, J. M. Gambetta, J. M. Chow, and B. R. Johnson, "Demonstration of quantum advantage in machine learning," *npj Quantum Information*, 2017.

[14] IBM Quantum, "IBM Quantum," <https://www.ibm.com/quantum>, 2025, accessed: 2025-08-04.

[15] Amazon Web Services, "Amazon braket," <https://aws.amazon.com/braket/>, 2025, accessed: 2025-08-04.

[16] Microsoft Azure, "Azure Quantum," <https://azure.microsoft.com/en-us/products/quantum>, 2025, accessed: 2025-08-04.

[17] S. Kundu and S. Ghosh, "Striq: Safeguarding training and inferencing of quantum neural networks from untrusted cloud," in *IEEE International Symposium on Hardware Oriented Security and Trust (HOST)*, 2025.

[18] S. Kundu and S. Ghosh, "Sok paper: Security concerns in quantum machine learning as a service," in *Proceedings of the International Workshop on Hardware and Architectural Support for Security and Privacy*, 2024, pp. 28–36.

[19] J. Chen and J. Szefer, "All your base are belong to us: Stealing vrp secrets from quantum circuit structures," in *IEEE International Symposium on Hardware Oriented Security and Trust (HOST)*, 2024.

[20] Y. Tan and J. Szefer, "I know what you are reading: Evaluating readout crosstalk in cloud-based quantum computers," in *Quantum Security and Privacy Workshop*, 2025.

[21] N. Choudhury, C. N. Mude, S. Das, P. C. Tikkireddi, S. Tannu, and K. Basu, "Crosstalk-induced side channel threats in multi-tenant nisq computers," in *Network and Distributed System Security (NDSS) Symposium*, 2025.

[22] C. Lu, E. Telang, A. Aysu, and K. Basu, "Quantum Leak: Timing side-channel attacks on cloud-based quantum services," in *Proceedings of the Great Lakes Symposium on VLSI (GLSVLSI)*, 2025.

[23] Y. Tan, N. Choudhury, K. Basu, and J. Szefer, "QubitHammer Attacks: Qubit flipping attacks in multi-tenant superconducting quantum computers," *arXiv preprint arXiv:2504.07875*, 2025.

[24] T. Lubinski, C. Granade, A. Anderson, A. Geller, M. Roetteler, A. Petrenko, and B. Heim, "Advancing hybrid quantum–classical computation with real-time execution," *Frontiers in Physics*, 2022.

[25] W. Gong and D.-L. Deng, "Universal adversarial examples and perturbations for quantum classifiers," *National Science Review*, 2022.

[26] M. T. West, S. M. Erfani, C. Leckie, M. Sevior, L. C. Hollenberg, and M. Usman, "Benchmarking adversarially robust quantum machine learning at scale," *Physical Review Research*, 2023.

[27] S. Kundu and S. Ghosh, "Adversarial data poisoning attack on quantum machine learning in the nisq era," in *Great Lakes Symposium on VLSI (GLSVLSI)*, 2025.

[28] J. Zhao, L. Yan, D. Tan, Y. Chang, and S. Zhang, "A black-box backdoor attack against quantum neural networks," *Quantum Science and Technology*, 2025.

[29] J. Guo, W. Jiang, R. Zhang, W. Fan, J. Li, G. Lu, and H. Li, "Backdoor attacks against hybrid classical-quantum neural networks," *Neural Networks*, 2025.

[30] C. Chu, L. Jiang, M. Swany, and F. Chen, "Qtrojan: A circuit backdoor against quantum neural networks," in *IEEE International Conference on Acoustics, Speech and Signal Processing (ICASSP)*, 2023.

[31] C. Xu, J. Sikora, and J. Szefer, "A thorough study of state leakage mitigation in quantum computing with one-time pad," in *IEEE International Symposium on Hardware Oriented Security and Trust (HOST)*, 2024.

[32] A. Ash-Saki, M. Alam, and S. Ghosh, "Analysis of crosstalk in NISQ devices and security implications in multi-programming regime," in *ACM/IEEE International Symposium on Low Power Electronics and Design (ISLPED)*, 2020.

[33] P. Murali, D. C. McKay, M. Martonosi, and A. Javadi-Abhari, "Software mitigation of crosstalk on noisy intermediate-scale quantum computers," in *International Conference on Architectural Support for Programming Languages and Operating Systems (ASPLOS)*, 2020.

[34] P. Zhao, "Mitigation of quantum crosstalk in cross-resonance-based qubit architectures," *Physical Review Applied*, 2023.

[35] C. Xu, F. Erata, and J. Szefer, "Exploration of power side-channel vulnerabilities in quantum computer controllers," in *ACM SIGSAC Conference on Computer and Communications Security (CCS)*, 2023.

[36] F. Erata, C. Xu, R. Piskac, and J. Szefer, "Quantum circuit reconstruction from power side-channel attacks on quantum computer controllers," *IACR Transactions on Cryptographic Hardware and Embedded Systems (TCHES)*, 2024.

[37] F. Chen, L. Jiang, H. Müller, P. Richerme, C. Chu, Z. Fu, and M. Yang, "Nisq quantum computing: A security-centric tutorial and survey," *IEEE Circuits and Systems Magazine*, 2024.

[38] C. Xu, J. Chen, A. Mi, and J. Szefer, "Securing nisq quantum computer reset operations against higher energy state attacks," in *ACM SIGSAC Conference on Computer and Communications Security (CCS)*, 2023.

[39] C. Xu, F. Erata, and J. Szefer, "Quantum computer fault injection attacks," in *IEEE International Conference on Quantum Computing and Engineering (QCE)*, 2024.

[40] C. Xu and J. Szefer, "Security attacks abusing pulse-level quantum circuits," in *IEEE Symposium on Security and Privacy (S&P)*, 2025.

[41] S. Lu, L.-M. Duan, and D.-L. Deng, "Quantum adversarial machine learning," *Physical Review Research*, 2020.

[42] J. Zheng, Z. He, and Z. Lin, "Hybrid adversarial sample crafting for black-box evasion attack," in *International Conference on Wavelet Analysis and Pattern Recognition (ICWAPR)*, 2017.

[43] A. S. Bhatia, S. Kais, and M. A. Alam, "Robustness of quantum federated learning (qfl) against "label flipping attacks" for lithography hotspot detection in semiconductor manufacturing," in *IEEE International Reliability Physics Symposium (IRPS)*, 2024.

[44] C. Szegedy, V. Vanhoucke, S. Ioffe, J. Shlens, and Z. Wojna, "Rethinking the inception architecture for computer vision," *IEEE Conference on Computer Vision and Pattern Recognition (CVPR)*, 2015.

[45] H. He, X. Lin, J. Chen, and Y. Xiao, "Q-Detection: A quantum-classical hybrid poisoning attack detection method," in *International Joint Conference on Artificial Intelligence (IJCAI)*, 2025.

[46] A. Madry, A. Makelov, L. Schmidt, D. Tsipras, and A. Vladu, "Towards deep learning models resistant to adversarial attacks," in *International Conference on Learning Representations (ICLR)*, 2018.

[47] I. J. Goodfellow, J. Shlens, and C. Szegedy, "Explaining and harnessing adversarial examples," in *International Conference on Learning Representations (ICLR)*, 2015.

[48] M. A. Nielsen and I. L. Chuang, *Quantum computation and quantum information*. Cambridge university press, 2010.

[49] E. Peters, J. Caldeira, A. Ho, S. Leichenauer, M. Mohseni, H. Neven, P. Spentzouris, D. Strain, and G. N. Perdue, "Machine learning of high dimensional data on a noisy quantum processor," *npj Quantum Information*, 2021.

[50] M. Benedetti, E. Lloyd, S. Sack, and M. Fiorentini, "Parameterized quantum circuits as machine learning models," *Quantum Science and Technology*, vol. 4, no. 4, p. 043001, 2019.

[51] A. Kandala, A. Mezzacapo, K. Temme, M. Takita, M. Brink, J. M. Chow, and J. M. Gambetta, "Hardware-efficient variational quantum eigensolver for small molecules and quantum magnets," *Nature*, 2017.

[52] M. Cerezo, A. Arrasmith, R. Babbush, S. C. Benjamin, S. Endo, K. Fujii, J. R. McClean, K. Mitarai, X. Yuan, L. Cincio *et al.*, "Variational quantum algorithms," *Nature Reviews Physics*, 2021.

[53] I. Cong, S. Choi, and M. D. Lukin, "Quantum convolutional neural networks," *Nature Physics*, 2019.

[54] S. Lloyd, M. Schuld, A. Ijaz, J. Izaac, and N. Killoran, "Quantum embeddings for machine learning," *arXiv preprint arXiv:2001.03622*, 2020.

[55] N. Dowling, M. T. West, A. Southwell, A. C. Nakhl, M. Sevior, M. Usman, and K. Modi, “Adversarial robustness guarantees for quantum classifiers,” *arXiv preprint arXiv:2405.10360*, 2024.

[56] M. Zomorodi, H. Amini, M. Abbaszadeh, J. Sohrabi, V. Salari, and P. Plawiak, “Optimal quantum circuit design via unitary neural networks,” *arXiv preprint arXiv:2408.13211*, 2024.

[57] F. C. Peres, “Pauli-based model of quantum computation with higher-dimensional systems,” *Physical Review A*, 2023.

[58] M. Kohda, R. Imai, K. Kanno, K. Mitarai, W. Mizukami, and Y. O. Nakagawa, “Quantum expectation-value estimation by computational basis sampling,” *Physical review research*, 2022.

[59] S. Patel, P. Jayakumar, T.-C. Yen, and A. F. Izmaylov, “Quantum measurement for quantum chemistry on a quantum computer,” *Chemical Reviews*, 2025.

[60] J. Preskill, “Quantum computing in the nisq era and beyond,” *Quantum*, 2018.

[61] S. Kundu, D. Kundu, and S. Ghosh, “Evaluating efficacy of model stealing attacks and defenses on quantum neural networks,” in *Proceedings of the Great Lakes Symposium on VLSI (GLSVLSI)*, 2024.

[62] Z. Fu, L. Zhao, X. Zhang, Y. Xu, G. Huang, and F. Chen, “CopyQNN: Quantum Neural Network Extraction Attack under Varying Quantum Noise,” in *International Joint Conference on Neural Networks (IJCNN)*, 2025.

[63] Z. Fu, M. Yang, C. Chu, Y. Xu, G. Huang, and F. Chen, “Quantumleak: Stealing quantum neural networks from cloud-based nisq machines,” in *International Joint Conference on Neural Networks (IJCNN)*, 2024.

[64] W. M. Watkins, S. Y.-C. Chen, and S. Yoo, “Quantum machine learning with differential privacy,” *Scientific Reports*, 2023.

[65] S. Bhowmik, T. S. Humble, and H. Thapliyal, “Quantum properties trojans (qupts) for attacking quantum neural networks,” in *IEEE Computer Society Annual Symposium on VLSI (ISVLSI)*, 2025.

[66] A. Ghosh and S. Ghosh, “Ai-driven reverse engineering of qml models,” in *International Symposium on Quality Electronic Design (ISQED)*. IEEE, 2025.

[67] A. Ghosh and S. Ghosh, “The quantum imitation game: Reverse engineering of quantum machine learning models,” in *Workshop on Attacks and Solutions in Hardware Security (ASHES)*, 2024.

[68] R. Roy, S. Das, and S. Ghosh, “Hardware trojans in quantum circuits, their impacts, and defense,” in *International Symposium on Quality Electronic Design (ISQED)*, 2024.

[69] J. Heredge, N. Kumar, D. Herman, S. Chakrabarti, R. Yalovetzky, S. H. Sureshbabu, C. Li, and M. Pistoia, “Characterizing privacy in quantum machine learning,” *npj Quantum Information*, 2025.

[70] Z. Wang, J. Li, Z. Hu, B. Gage, E. Iwasawa, and W. Jiang, “Qumos: A framework for preserving security of quantum machine learning model,” in *IEEE International Conference on Quantum Computing and Engineering (QCE)*, 2023.

[71] J. Watrous, *The Theory of Quantum Information*, 2018.

[72] M. A. Nielsen and I. L. Chuang, *Quantum Computation and Quantum Information*, 2010.

[73] S. Kundu and S. Ghosh, “Adversarial data poisoning attack on quantum machine learning in the NISQ era,” in *Great Lakes Symposium on VLSI (GLSVLSI)*, 2025.

[74] S. M. Saeed, R. Wille, and R. Karri, “Locking the design of building blocks for quantum circuits,” *ACM Transactions on Embedded Computing Systems (TECS)*, 2019.

[75] A. Rehman, V. Langford, J. John, and Y. Liu, “OPAQUE: Obfuscating phase in quantum circuit compilation for efficient ip protection,” in *International Symposium on Quality Electronic Design (ISQED)*, 2025.

[76] L. Deng, “The MNIST database of handwritten digit images for machine learning research [best of the web],” *IEEE Signal Processing Magazine*, 2012.

[77] M. S. Rahman, S. Coull, Q. Yu, and M. Wright, “MADAR: Efficient continual learning for malware analysis with diversity-aware replay,” in *Conference on Applied Machine Learning in Information Security (CAMLIS)*. PMLR, 2025.

[78] V. Bergholm, J. Izaac, M. Schuld, C. Gogolin, S. Ahmed, V. Ajith, M. S. Alam, G. Alonso-Linaje, B. AkashNarayanan, A. Asadi *et al.*, “Pennylane: Automatic differentiation of hybrid quantum-classical computations,” *arXiv preprint arXiv:1811.04968*, 2018.

[79] G. Aleksandrowicz, T. Alexander, P. Barkoutsos, L. Bello, Y. Ben-Haim, D. Bucher, F. J. Cabrera-Hernández, A. Carballo Franquis, C. Chen, J. Chen *et al.*, “Qiskit: An open-source framework for quantum computing,” *Zenodo*, 2019.

[80] S. Sim, P. D. Johnson, and A. Aspuru-Guzik, “Expressibility and entangling capability of parameterized quantum circuits for hybrid quantum-classical algorithms,” *Advanced Quantum Technologies*, 2019.

[81] S. Lu, L.-M. Duan, and D.-L. Deng, “Quantum adversarial machine learning,” *Phys. Rev. Res.*, 2020.

[82] X. Jiang, K. Wang, K. Qian, Z. Chen, Z. Chen, L. Lu, L. Xia, F. Song, S. Zhu, and X. Ma, “Towards the standardization of quantum state verification using optimal strategies,” *npj Quantum Information*, 2020.

[83] X.-D. Yu, J. Shang, and O. Gühne, “Statistical methods for quantum state verification and fidelity estimation,” *Advanced Quantum Technologies*, 2022.

[84] A. Govindankutty and S. K. Srinivasan, “Superposition-based abstractions for quantum data encoding verification,” *IET Quantum Communication*, 2025.

[85] W. Gong, D. Yuan, W. Li, and D.-L. Deng, “Enhancing quantum adversarial robustness by randomized encodings,” *Physical Review Research*, 2024.

[86] S. Das and S. Ghosh, “Randomized reversible gate-based obfuscation for secured compilation of quantum circuit,” *arXiv preprint arXiv:2305.01133*, 2023.

[87] T. Kit, K. Pov, K. Kea, W.-D. Chang, H. Chul Park, and Y. Han, “Enhancing a convolutional autoencoder with a quantum approximate optimization algorithm for image noise reduction,” *Machine Learning: Science and Technology*, 2025.

[88] R. O. Topaloglu, “Quantum logic locking for security,” *J*, 2023.

[89] A. Raj and V. Balachandran, “Quantum opacity, classical clarity: A hybrid approach to quantum circuit obfuscation,” *arXiv preprint arXiv:2505.13848*, 2025.

[90] S. Tan, D. Xiang, L. Lu, J. Lu, Q. Jiang, M. Chen, and J. Yin, “MorphQPV: Exploiting isomorphism in quantum programs to facilitate confident verification,” in *International Conference on Architectural Support for Programming Languages and Operating Systems (ASPLOS)*, 2024.

[91] Y. Liu, J. John, and Q. Wang, “E-loq: Enhanced locking for quantum circuit ip protection,” in *IEEE International Symposium on Hardware Oriented Security and Trust (HOST)*, 2025.

[92] A. Suresh, A. A. Saki, M. Alam, R. Onur Topaloglu, and S. Ghosh, “Short paper: A quantum circuit obfuscation methodology for security and privacy,” in *International Workshop on Hardware and Architectural Support for Security and Privacy (HASP)*, 2021.

[93] P. Murali, D. C. McKay, M. Martonosi, and A. Javadi-Abhari, “Software mitigation of crosstalk on noisy intermediate-scale quantum computers,” in *International Conference on Architectural Support for Programming Languages and Operating Systems (ASPLOS)*, 2020.

[94] L. Xie, J. Zhai, and W. Zheng, “Mitigating crosstalk in quantum computers through commutativity-based instruction reordering,” in *ACM/IEEE Design Automation Conference (DAC)*, 2021.

[95] B. Harper, B. Tonekaboni, B. Goldozian, M. Sevior, and M. Usman, “Crosstalk attacks and defence in a shared quantum computing environment,” *Advanced Quantum Technologies*, 2025.

[96] D. Mehra and A. Kaley, “Defending crosstalk-mediated quantum attacks using dynamical decoupling,” *arXiv preprint arXiv:2409.14598*, 2024.

[97] Y. Zhang, Y. Zhang, S. Li, W. Zheng, and Y. Yu, “Diagnosing quantum crosstalk in superconducting quantum chips by using out-of-time-order correlators,” *Chinese Physics B*, 2024.

[98] N. Choudhury and K. Basu, “A survey of side-channel attacks in superconducting quantum computers,” in *IEEE Computer Society Annual Symposium on VLSI (ISVLSI)*, 2024.

## X. APPENDIX

### A. QMLP Baseline

This section presents the extended results for baseline and the QMLP models under two conditions: noiseless simulation and depolarizing noise with probability  $p = 0.01$ . Results are shown for AZ-Class and MNIST datasets, considering two encoding strategies (Angle and Amplitude) and varying circuit depths. **E.:** Encoding, **L:** Number of Layers, **Acc.:** Accuracy, **F1:** F1-Score, **FPR:** False Positive Rate, and **FNR:** False Negative Rate.

TABLE VII: QMLP Baseline under Noiseless Condition.

	E.	L	Acc.	F1	FPR	FNR
AZ-Class	Angle	2	49.77	48.41	2.29	50.88
		5	52.25	50.60	2.17	48.55
		10	54.88	53.18	2.05	45.89
		50	32.39	29.46	3.09	69.57
		2	40.11	38.74	2.73	60.48
	Amplitude	5	48.11	45.62	2.37	52.64
		10	55.04	53.88	2.05	45.83
		50	66.90	65.30	1.51	34.27
		2	66.0	65.2	3.8	34.6
		5	67.99	67.32	3.56	32.59
MNIST	Angle	10	71.72	83.63	3.14	28.80
		50	76.89	76.61	2.57	23.46
		2	50.74	49.50	5.47	49.91
		5	70.27	69.84	3.30	30.17
		10	79.82	79.56	2.24	20.47
	Amplitude	50	92.64	92.56	0.82	7.44
		2				
		5				
		10				
		50				

Table VII presents the QMLP baseline performance under ideal noiseless conditions. For both datasets, increasing the number of layers improves accuracy with amplitude encoding consistently outperforming angle encoding. On AZ-Class the model reaches moderate performance, peaking with 66.90% using amplitude encoding and 50 layers. In contrast, MNIST shows a much stronger response to circuit depth, with amplitude encoding achieving over 92% accuracy on 50 layers.

TABLE VIII: QMLP Baseline under Depolarized Noise  $p = 0.01$ .

	E.	L	Acc.	F1	FPR	FNR
AZ-Class	Angle	2	46.7	48.0	2.4	55.8
		5	21.4	25.6	3.6	80.9
		10	4.9	0.9	4.3	95.6
		50	5.1	4.0	4.3	95.4
	Amplitude	2	5.1	2.0	4.3	95.5
		5	5.0	1.5	4.3	95.5
		10	4.8	4.1	4.3	95.6
		50	4.8	3.9	4.3	95.7
		2				
MNIST	Angle	5	59.2	60.0	4.5	41.2
		10	40.9	48.2	6.5	59.0
		50	23.6	24.9	8.5	76.6
		2	9.9	9.7	10.0	90.1
	Amplitude	5	9.5	6.8	10.0	90.1
		10	10.1	10.4	10.0	89.8
		50	9.7	9.2	10.0	90.2
		2				
		5				
		10				
		50				

Table VIII shows the QMLP baseline performance under depolarizing noise with  $p = 0.01$ . Compared to the noiseless setting, both AZ-Class and MNIST suffer substantial accuracy drops, as the circuit depth increases. For AZ-Class, angle and amplitude encoding reach as low as 5.1% and 4.8% respectively. MNIST also experiences something similar, where accuracy falls below 10% for deeper circuits under both encodings.

TABLE X: CMLP under FGSM attacks.

Dataset	Attack	Acc.	F1	FPR/FNR
MNIST	None	96.63	96.59	0.36/3.28
	FGSM ( $\epsilon = 0.01$ )	94.18	94.11	0.64/5.87
	FGSM ( $\epsilon = 0.1$ )	31.64	31.47	7.75/69.43
	FGSM ( $\epsilon = 0.15$ )	16.17	16.05	9.35/83.97
AZ_Class	None	95.89	94.35	0.16/6.06
	FGSM ( $\epsilon = 0.01$ )	93.11	90.44	0.27/10.01
	FGSM ( $\epsilon = 0.1$ )	28.32	17.95	2.86/81.03
	FGSM ( $\epsilon = 0.15$ )	12.15	6.20	3.59/94.27

TABLE IX: QMLP under FGSM attack in Noiseless Condition.

Encoding	Layers	Attack	MNIST			AZ-Class		
			MNIST			AZ-Class		
			Acc.	F1	FPR / FNR	Acc.	F1	FPR / FNR
Angle	2	None	66.0	65.2	3.8 / 34.6	49.8	48.4	2.3 / 50.9
		FGSM ( $\epsilon=0.01$ )	32.4	34.7	7.5 / 66.6	19.5	19.7	3.7 / 82.4
		FGSM ( $\epsilon=0.10$ )	3.3	3.5	10.7 / 96.6	15.8	15.3	3.9 / 85.8
		FGSM ( $\epsilon=0.15$ )	0.7	0.8	11.0 / 99.2	13.9	13.2	3.9 / 87.5
	5	None	68.0	67.3	3.6 / 32.6	52.3	50.6	2.2 / 48.6
		FGSM ( $\epsilon=0.01$ )	32.0	36.5	7.5 / 67.0	15.0	15.0	3.9 / 86.4
		FGSM ( $\epsilon=0.10$ )	2.7	2.9	10.8 / 97.3	12.0	11.6	4.0 / 89.1
		FGSM ( $\epsilon=0.15$ )	1.0	1.0	11.0 / 99.0	10.4	9.9	4.1 / 90.6
	10	None	71.7	71.2	3.1 / 28.8	54.8	53.5	2.1 / 45.8
		FGSM ( $\epsilon=0.01$ )	27.1	34.0	8.0 / 71.8	15.4	14.7	3.9 / 86.0
		FGSM ( $\epsilon=0.10$ )	3.8	3.7	10.6 / 96.0	12.1	11.1	4.0 / 89.0
		FGSM ( $\epsilon=0.15$ )	1.4	1.3	10.9 / 98.5	10.4	9.5	4.1 / 90.5
	50	None	76.9	76.6	2.6 / 23.5	32.4	29.5	3.1 / 69.6
		FGSM ( $\epsilon=0.01$ )	26.9	35.1	8.1 / 72.1	5.2	3.9	4.3 / 95.3
		FGSM ( $\epsilon=0.10$ )	5.7	6.0	10.4 / 94.0	5.0	4.2	4.3 / 95.4
		FGSM ( $\epsilon=0.15$ )	3.6	3.8	10.7 / 96.2	5.0	4.1	4.3 / 95.4
Amplitude	2	None	50.7	49.5	5.5 / 49.9	40.1	38.7	2.7 / 60.5
		FGSM ( $\epsilon=0.01$ )	15.1	12.8	9.4 / 84.4	13.7	12.9	3.9 / 87.2
		FGSM ( $\epsilon=0.10$ )	5.0	3.3	10.5 / 94.8	0.7	0.4	4.5 / 99.3
		FGSM ( $\epsilon=0.15$ )	2.2	1.4	10.8 / 97.7	0.4	0.2	4.5 / 99.7
	5	None	70.3	69.8	3.3 / 30.2	48.1	45.6	2.4 / 52.6
		FGSM ( $\epsilon=0.01$ )	17.0	21.3	9.2 / 82.6	13.6	15.1	3.9 / 86.6
		FGSM ( $\epsilon=0.10$ )	1.5	0.9	10.9 / 98.4	0.3	0.2	4.6 / 99.7
		FGSM ( $\epsilon=0.15$ )	0.5	0.3	11.0 / 99.4	0.1	0.1	4.6 / 99.9
	10	None	79.8	79.6	2.2 / 20.5	55.0	53.9	2.1 / 45.8
		FGSM ( $\epsilon=0.01$ )	22.3	25.0	8.6 / 77.6	15.8	16.5	3.8 / 84.7
		FGSM ( $\epsilon=0.10$ )	1.0	0.8	11.0 / 99.0	0.6	0.4	4.5 / 99.5
		FGSM ( $\epsilon=0.15$ )	0.1	0.1	11.1 / 99.9	0.1	0.1	4.6 / 99.9
	50	None	92.6	92.6	0.8 / 7.4	67.0	65.4	1.5 / 34.2
		FGSM ( $\epsilon=0.01$ )	27.3	32.6	8.1 / 72.6	18.0	19.5	3.7 / 82.5
		FGSM ( $\epsilon=0.10$ )	0.0	0.0	11.1 / 100.0	0.0	0.0	4.6 / 100.0
		FGSM ( $\epsilon=0.15$ )	0.0	0.0	11.1 / 100.0	0.0	0.0	4.6 / 100.0

### B. QMLP under FGSM and PGD Attacks

This section presents extended results from QMLP against gradient-based adversarial perturbations. We report performance of FGSM and PGD for both datasets and encoding schemes.

Table IX summarizes the behavior of QMLP under FGSM attacks of increasing perturbation strength ( $\epsilon$ ) for the MNIST and AZ-Class datasets. Results are provided for both angle and amplitude encoded models with varying circuit depths. Table X summarizes behaviour for the CMLP under FGSM attack, for the MNIST and AZ-Class dataset. **Acc.:** Accuracy, **F1:** F1-Score, **FPR:** False Positive Rate, and **FNR:** False Negative Rate.

Table XII shows the performance of the QMLP under PGD attacks in noiseless condition. Table XIII summarizes behaviour for the CMLP under PGD attack.

TABLE XI: QMLP–Amplitude: Accuracy and F1 ratios under PGD attacks (relative to no-attack case).

Layers	Attack	MNIST (ratio)		AZ-Class (ratio)	
		Acc.	F1	Acc.	F1
2	PGD ( $\epsilon=0.01$ )	0.274	0.232	0.327	0.318
	PGD ( $\epsilon=0.10$ )	0.032	0.014	0.005	0.003
	PGD ( $\epsilon=0.15$ )	0.004	0.002	0.000	0.000
10	PGD ( $\epsilon=0.01$ )	0.241	0.269	0.258	0.276
	PGD ( $\epsilon=0.10$ )	0.001	0.001	0.002	0.000
	PGD ( $\epsilon=0.15$ )	0.000	0.000	0.000	0.000
50	PGD ( $\epsilon=0.01$ )	0.237	0.282	0.230	0.251
	PGD ( $\epsilon=0.10$ )	0.000	0.000	0.000	0.000
	PGD ( $\epsilon=0.15$ )	0.000	0.000	0.000	0.000

TABLE XII: QMLP under PGD attack in Noiseless Condition.

Encoding	Layers	Attack	MNIST			AZ-Class		
			Acc.	F1	FPR / FNR	Acc.	F1	FPR / FNR
Angle	2	None	66.0	65.2	3.8 / 34.6	49.8	48.4	2.3 / 50.9
		PGD ( $\epsilon=0.01$ )	31.9	35.3	7.5 / 67.1	19.4	19.8	3.7 / 82.5
		PGD ( $\epsilon=0.10$ )	2.7	2.7	10.8 / 97.2	15.4	15.1	3.9 / 86.2
		PGD ( $\epsilon=0.15$ )	0.3	0.3	11.0 / 99.7	13.1	12.6	4.0 / 88.2
5	5	None	68.0	67.3	3.6 / 32.6	52.3	50.6	2.2 / 48.6
		PGD ( $\epsilon=0.01$ )	31.2	36.3	7.6 / 67.8	14.9	14.9	3.9 / 86.4
		PGD ( $\epsilon=0.10$ )	1.6	1.6	10.9 / 98.4	11.2	10.8	4.1 / 89.8
		PGD ( $\epsilon=0.15$ )	0.2	0.2	11.0 / 99.8	9.4	9.0	4.1 / 91.5
10	10	None	71.7	71.2	3.1 / 28.8	54.8	53.5	2.1 / 45.8
		PGD ( $\epsilon=0.01$ )	26.3	33.2	8.1 / 72.7	15.3	14.6	3.9 / 86.1
		PGD ( $\epsilon=0.10$ )	2.6	1.9	10.8 / 97.2	11.3	10.8	4.1 / 89.7
		PGD ( $\epsilon=0.15$ )	0.6	0.3	11.0 / 99.3	9.4	8.8	4.1 / 91.4
50	50	None	76.9	76.6	2.6 / 23.5	32.4	29.5	3.1 / 69.6
		PGD ( $\epsilon=0.01$ )	25.4	32.7	8.2 / 73.6	4.2	3.5	4.4 / 96.2
		PGD ( $\epsilon=0.10$ )	2.6	2.8	10.8 / 97.4	1.1	0.7	4.5 / 99.0
		PGD ( $\epsilon=0.15$ )	0.7	0.7	11.0 / 99.2	0.6	0.4	4.5 / 99.5
Amplitude	2	None	50.7	49.5	5.5 / 49.9	40.1	38.7	2.7 / 60.5
		PGD ( $\epsilon=0.01$ )	13.9	11.5	9.5 / 85.6	13.1	12.3	4.0 / 87.7
		PGD ( $\epsilon=0.10$ )	1.6	0.7	10.9 / 98.4	0.2	0.1	4.5 / 99.8
		PGD ( $\epsilon=0.15$ )	0.2	0.1	11.1 / 99.8	0.0	0.0	4.5 / 100.0
5	5	None	70.3	69.8	3.3 / 30.2	48.1	45.6	2.4 / 52.6
		PGD ( $\epsilon=0.01$ )	14.9	18.3	9.4 / 84.7	12.4	14.0	4.0 / 87.7
		PGD ( $\epsilon=0.10$ )	0.0	0.0	11.1 / 100.0	0.0	0.0	4.6 / 100.0
		PGD ( $\epsilon=0.15$ )	0.0	0.0	11.1 / 100.0	0.0	0.0	4.6 / 100.0
10	10	None	79.8	79.6	2.2 / 20.5	55.0	53.9	2.1 / 45.8
		PGD ( $\epsilon=0.01$ )	19.2	21.4	9.0 / 80.7	14.2	14.9	3.9 / 86.2
		PGD ( $\epsilon=0.10$ )	0.1	0.1	11.1 / 99.9	0.1	0.0	4.6 / 99.9
		PGD ( $\epsilon=0.15$ )	0.0	0.0	11.1 / 100.0	0.0	0.0	4.6 / 100.0
50	50	None	92.6	92.6	0.8 / 7.4	67.0	65.4	1.5 / 34.2
		PGD ( $\epsilon=0.01$ )	21.9	26.1	8.7 / 77.9	15.4	16.4	3.9 / 84.8
		PGD ( $\epsilon=0.10$ )	0.0	0.0	11.1 / 100.0	0.0	0.0	4.6 / 100.0
		PGD ( $\epsilon=0.15$ )	0.0	0.0	11.1 / 100.0	0.0	0.0	4.6 / 100.0

TABLE XIII: CMLP under PGD attacks.

Dataset	Attack	Acc.	F1	FPR/FNR
MNIST	None	96.33	96.59	0.36/3.28
	PGD ( $\epsilon = 0.01$ )	94.05	93.98	0.66/5.99
	PGD ( $\epsilon = 0.1$ )	9.01	9.25	10.11/90.97
	PGD ( $\epsilon = 0.15$ )	1.91	1.73	10.79/97.23
AZ_Class	None	95.89	94.35	0.16/6.06
	PGD ( $\epsilon = 0.01$ )	92.88	90.14	0.16/6.06
	PGD ( $\epsilon = 0.1$ )	9.91	4.79	3.63/95.48
	PGD ( $\epsilon = 0.15$ )	2.30	0.96	3.94/99.36

### C. Label Flipping Attacks

Table XIV and Table XV summarizes the behavior of QMLP under 50% untargeted label-Flipping attack in noiseless condition and depolarized noise ( $p = 0.01$ ) condition respectively. **E.**: Encoding, **L**: Layer, **LS**: Label-Smoothing, **Acc.**: Accuracy.

TABLE XIV: QMLP under Label-Flipping attack in noiseless condition.

E.	L	LS	AZ-Class Dataset				MNIST Dataset			
			Acc.	F1	FNR	FPR	Acc.	F1	FNR	FPR
Angle	2	Y	44.81	41.11	57.57	2.25	60.73	60.89	39.81	4.35
	5	Y	47.56	43.68	53.53	2.38	64.28	63.91	36.21	3.97
	10	Y	48.70	44.76	54.38	2.37	65.72	65.19	35.33	3.86
	2	N	46.42	43.19	55.53	2.42	61.43	61.38	38.53	4.21
Amplitude	5	N	47.57	44.05	53.27	2.35	64.43	64.10	35.99	3.93
	10	N	49.93	45.81	51.09	2.26	66.43	65.84	34.63	3.79
	2	Y	34.93	28.98	66.45	2.94	53.93	50.53	46.96	5.09
	10	Y	50.24	43.37	48.88	2.16	78.17	77.66	2.56	2.24
50	Y	60.57	53.88	40.08	1.76	89.61	89.47	10.35	1.12	
	2	N	37.64	33.21	62.42	2.80	52.32	48.89	47.64	5.18
	10	N	50.76	45.66	49.67	2.20	75.95	75.27	23.79	2.59
	50	N	62.39	56.60	38.58	1.69	90.09	89.96	9.65	1.05

TABLE XV: QMLP under Label-Flipping attack with evaluation on Depolarization Noise ( $p = 0.01$ ).

Angle	E.	L	LS	AZ Dataset				MNIST Dataset			
				Acc.	F1	FNR	FPR	Acc.	F1	FNR	FPR
2	2	Y	40.73	33.74	61.07	2.70	48.72	47.09	52.27	5.74	
	5	Y	16.62	12.71	85.06	3.81	28.33	22.51	72.98	8.05	
	10	Y	9.80	3.75	90.93	4.12	13.07	4.80	87.22	9.66	
	2	N	44.49	37.73	57.53	2.53	52.37	50.58	48.56	5.32	
5	5	N	38.84	31.91	62.52	2.78	45.13	39.97	56.01	6.12	
	10	N	16.30	10.79	85.39	3.82	17.18	8.40	83.47	9.23	
	2	Y	5.24	1.16	95.31	4.33	10.00	3.24	90.11	10.01	
	10	Y	5.01	2.18	95.52	4.34	9.96	3.79	89.89	9.98	
50	Y	4.73	3.20	95.73	4.35	10.20	8.76	89.65	9.96		
	2	N	5.58	1.49	95.01	4.31	9.71	3.83	89.82	9.98	
	10	N	4.91	0.72	95.61	4.34	9.64	2.80	90.14	10.01	
	50	N	4.83	3.19	95.63	4.34	9.85	7.38	90.01	10.00	

### D. QNN under QUID and Q-detection

This section summarizes the 4-Class classification accuracy of QNN model under QUID attacks with and without Q-Detection as defense, for both noiseless and noisy simulation settings respectively in Table XVI and Table XVII.

TABLE XVI: QUID Accuracy on AZ-Class and MNIST with and without Q-detection in noiseless settings.

Poison Ratio	Attack Type	AZ-Class		MNIST(%)	
		w/o Q-det	w/ Q-det	w/o Q-det	w/ Q-det
0.1	Random	61.3	59.7	58.3	54.7
	QUID	64.0	58.0	60.7	57.0
0.3	Random	57.7	52.6667	57.7	61.7
	QUID	45.7	47.7	54.0	42.7
0.5	Random	51.7	51.0	58.3	56.0
	QUID	27.0	10.0	5.7	7.0
0.7	Random	26.0	28.7	40.7	39.0
	QUID	6.0	7.0	4.77	4.0

TABLE XVII: QUID Accuracy on AZ-Class and MNIST with and without Q-detection in noisy settings.

Poison Ratio	Attack Type	AZ-Class		MNIST	
		w/o Q-det	w/ Q-det	w/o Q-det	w/ Q-det
0.1	Random	25.0	25.0	25.0	25.0
	QUID	25.0	25.7	25.0	25.7
0.3	Random	26.0	25.0	25.0	25.0
	QUID	25.0	25.0	25.0	25.0
0.5	Random	24.7	27.7	25.0	25.0
	QUID	25.0	25.0	25.0	25.0
0.7	Random	25.0	25.0	25.0	25.0
	QUID	25.0	25.0	25.0	22.0